

# The influence of inlet velocity profile and secondary flow on pulsatile flow in a model artery with stenosis

SEAN D. PETERSON† AND MICHAEL W. PLESNIAK

Department of Mechanical Engineering, Purdue University, West Lafayette, IN 47907, USA  
plesniak@purdue.edu

(Received 30 May 2007 and in revised form 3 July 2008)

The results of an experimental investigation to determine the influence of two physiologically relevant inlet conditions on the flow physics downstream of an idealized stenosis are presented. The two inlet conditions are an asymmetric mean inlet velocity profile and an asymmetric mean inlet velocity profile plus secondary flow, as found downstream of a bend. The stenosis is modelled as an axisymmetric 75% area reduction occlusion with a length-to-diameter ratio of 2. The flow was forced by a 10-harmonic carotid artery-inspired waveform with mean, maximum and minimum Reynolds numbers of 364, 1424 and 24, respectively, and a Womersley number of 4.6. Laser Doppler velocimetry and particle image velocimetry were used to characterize the spatial and temporal evolution of a baseline case (no disturbances) as well as the two physiologically relevant inlet conditions. The asymmetric inlet velocity profile was found to reduce the region of influence of the stenosis by forcing the stenotic jet towards the tube wall via an induced non-uniform radial pressure gradient, similar to the Coanda effect. Curvature-induced secondary flow was found to play a minor role in the near-stenosis region. Vortex ring formation was relatively unaffected by the mean velocity gradient and secondary flow. Evidence of remnants of the starting vortex ring was observed far downstream in all cases.

---

## 1. Introduction

The American Heart Association recently reported that 71 million Americans suffer from cardiovascular disease (Thom *et al.* 2006). Evidence linking cellular biochemical response to mechanical factors such as shear stress on the endothelial cells lining the arterial wall has resulted in a surge in research efforts aimed at understanding the fluid mechanics of the vasculature and the impact of pathologies (see Frangos, McIntire & Eskin 1988; Ku 1997; Topper & Gimbrone Jr. 1999; Berger & Jou 2000; Stroud, Berger & Saloner 2002; Hsiai *et al.* 2002, 2003; Tarbell, Weinbaum & Kamm 2005). Mechanisms of force detection and mechanotransduction, the transformation of forces applied to cells into biochemical responses by cells, are relatively poorly understood. Seminal work by Dewey *et al.* (1981) and Nerem, Levesque & Cornhill (1981) on the morphology of endothelial cells demonstrating that the cells aligned in the direction of shear stress indicated that cells are dynamic, responding to their hemodynamic environment. The inter-relation between forces and biochemical response are now known to be fascinatingly complex (Kamm 2002; Tarbell *et al.*

† Present address: Polytechnic University, 6 MetroTech Center RH513, Brooklyn, NY, 11201, USA.

2005; Tarbell & Phakis 2006). Wall shear stress, in particular, has been shown to regulate atheroprotective functions via several chemical mediators (Frangos *et al.* 1988; Tarbell *et al.* 2005). The mechanisms by which endothelial cells detect shear stress is the subject of intense theoretical and experimental investigation. There is strong evidence suggesting that the glycocalyx, a thin coating of macromolecules lining and the luminal face of the endothelial cell monolayer, may play a key role in sensing the hemodynamic environment (Tarbell *et al.* 2005; Tarbell & Phakis 2006). McCann (2005) investigated endothelial cell response to stenotic flow in a steady, axisymmetric flow environment. McCann decomposed the post-stenotic region into near- and far-field zones. The near-field ranged from 0 to  $15D$  and the far-field stretched from  $15D$  to  $30D$ . The near-field region, which encompassed the recirculation and re-attachment regions, had atherogenic endothelial cell activation, while the character of the far-field was similar to that of the atheroprotective upstream. McCann *et al.* (2005) reported the sensitivity of endothelial cells to even small variations in shear stress that can occur in the parallel plate flow chambers typically employed in cellular studies.

Arterial flow is highly complex, involving pulsatile flow within curved, branching, elastic, tapered tubes. Flow is typically laminar, although other flow regimes can be induced by pathological vessel geometries and enhanced by the unsteady forcing. Up to eight harmonics of the primary waveform frequency are important to characterize the forcing (Ku 1997), and non-Newtonian effects can be significant in the small arteries and regions of low shear (Elad & Einav 2003).

Curvature in the vasculature is ubiquitous and can be dramatic in some arteries, e.g. the  $\sim 180^\circ$  aortic arch. Steady flow in curved tubes and channels was analysed by Dean (1928). His analysis of the centrifugal instability in a curved channel flow established conditions under which viscosity no longer sufficiently damps the inviscid instability and secondary flows develop. Dean's analysis was extended to zero-mean, sinusoidally oscillating flow in a curved pipe by Lyne (1970). Lyne assumed a thin Stokes layer and predicted a four-vortex secondary-flow system, where the counter-rotating vortices in the inviscid core rotated in the opposite sense to that of the steady flow Dean vortices. A second pair of counter-rotating vortices in the Stokes layer rotated in the conventional sense. Womersley (1955) discussed the importance of the ratio of Stokes layer thickness to the tube radius in his development of the analytical solution of pulsatile flow in a straight, rigid vessel. High Womersley number (defined as  $\alpha = R\sqrt{\omega/\nu}$ ) flows are inertially dominated and consequently have thin Stokes layers. The unsteady pipe flow problem was originally solved by Sexl and  $\alpha^2$  is sometimes referred to as the kinetic Reynolds number (White 2006).

Chandran *et al.* (1974) incorporated elastic walls into Lyne's analysis and found that the secondary flow streamlines were phase dependent. Flows in the Stokes layer and the inviscid core both changed directions several times, flowing in the same direction for about half of the cycle and in opposite directions for the other half. Lin & Tarbell (1980) studied non-zero mean oscillating flow and observed a resonance-like character between the axial and secondary flows. More recent numerical works on flow in curved tubes have examined larger curvature ratios (tube radius to radius of curvature,  $\delta/R$ ) and non-sinusoidal pulsing (Komai & Tanishita 1997). Experimental measurements of aortic arch models have been performed by several researchers confirming the predictions of Lyne and have also documented several higher order instability modes (Chandran 1993; Naruse & Tanishita 1996; Konno, Satoh & Tanishita 1999).

Development of steady flow in a curved tube shows that the flow initially favours the inner wall due to streamline curvature and then migrates to the outer wall because of the centrifugal acceleration (Berger, Talbot & Yao 1983; Snyder, Hammersley &

Olson 1985). Snyder *et al.* (1985) demonstrated that the development of laminar flow in a curved pipe is not a sole function of the Dean number, but rather certain modes exist in which the curvature ratio and Reynolds number are independently important. Once fully developed, the axial flow profile is roughly linear over the bulk of the flow cross-section. In pulsatile flow, Talbot & Gong (1983) found that the axial flow separated from the inner wall during deceleration, and they discovered the presence of helical structures in the Dean's vortices. Swanson, Stalp & Donnelly (1993) looked at flow development in curved pipes experimentally and suggested that flow becomes fully developed near  $165^\circ$  in a  $180^\circ$  bend. Komai & Tanishita (1997) simulated flow around a curved tube for several curvature ratios, Womersley numbers, and intermittency parameters (ratio of systolic time to the total cardiac period). They showed the nearly linear nature of the velocity profile at various phases and depicted the secondary flow structures for the various parameters. More recently, Dwyer *et al.* (2001) performed a study of unsteady flows in curved pipes and found that for Womersley numbers greater than about 15, the flow exhibits an inviscid-like nature, driven by the unsteady pressure field. They also found that during deceleration the flow near the inner wall is significantly retarded.

Unlike the studies of flow in curved vessels that typically focus on atherogenesis, the study of stenotic flows is concerned with the effect of developed lesions on the local hemodynamic environment. The local hemodynamics may impact plaque rupture, thrombus formation, and general vessel health distal to the stenosis (Nerem 1992). Stenoses are characterized by the degree of occlusion, typically in percent area compared with the unoccluded vessel. Stenoses with area reduction greater than 75 % are considered clinically significant, as they are at high risk of thrombus formation, rupture and ischemia.

Seminal work in the 1980s by Giddens using *in vitro* models characterized the mean flow field and frequency content as a function of Reynolds number in both steady and pulsatile flows (see Khalifa & Giddens 1981; Ahmed & Giddens 1983, 1984) in straight rigid vessels. The 75 % stenosis under steady flow or sinusoidal forcing investigated by Giddens has become a canonical stenotic flow. The mean and fluctuating flow field is well characterized and consequently this geometry has been used by many researchers as a baseline (Ojha *et al.* 1989; Siouffi, Deplano & Pelissier 1998; Cao & Rittgers 1998; Deplano & Siouffi 1999; Stroud, Berger & Saloner 2000; Long *et al.* 2001; Peterson & Plesniak 2003; Sherwin & Blackburn 2005; Varghese, Frankel & Fischer 2007*b*).

Advanced mesh generation schemes and powerful computers have resulted in a larger number of computational stenotic flow studies. High-level numerical experiments provide access to several quantities that are difficult to measure experimentally, such as time-resolved wall shear stress (WSS) and pressure distributions in realistic geometries. Hyun, Kleinstreuer & Archie Jr. 2000 examined axisymmetric and asymmetric expansions subjected to a physiologically relevant waveform. They mapped wall shear stress gradients and introduced a parameter, the wall shear stress angle deviation, that encompasses regions known to be atherogenic (i.e. low WSS) and those that are thrombogenic (i.e. high WSS). Stroud *et al.* (2000) determined that several factors such as surface irregularity, stenosis aspect ratio and the pulsatile waveform can play a significant role in stenotic flow physics. Long *et al.* (2001) demonstrated that asymmetric stenoses have a shorter zone of influence than axisymmetric stenoses, a fact also reported by Varghese *et al.* (2007*b*).

Mittal, Simmons & Udaykumar (2001) and Mittal, Simmons & Najjar (2003) used large eddy simulations (LES) to investigate turbulence production in stenotic

flows. Their study was performed in a channel with semicircular stenosis models and found that above a Reynolds number of approximately 1000 the flow transitions to turbulence. Sherwin & Blackburn (2005) investigated the three-dimensional instability mechanism of an axisymmetric stenotic flow to broad-spectrum velocity perturbations. They found that the starting vortex ring (at high enough Reynolds number) tilts and rapidly breaks down through its interaction with the wall. They predicted that transition can occur within a few diameters of the stenosis, in agreement with observation. Furthermore, Sherwin and Blackburn reported single-harmonic forcing to be more unstable than more complex input signals. Blackburn & Sherwin (2007) extended this work and found that a Widnall-type wavy vortex core instability mechanism can dominate at sufficiently high Reynolds numbers and low reduced velocities, whereas the vortex-tilting mode dominates at higher reduced velocities. They also observed that a convective shear layer instability can act as a destabilizing agent for the period-doubling vortex tilting instability at low Womersley number. Varghese *et al.* (2007*a,b*) demonstrated that a geometric perturbation (a slight displacement of the stenosis axis with respect to the tube axis, or eccentricity) is sufficient to induce turbulent transition in both steady and pulsatile flow where none had been observed in the axisymmetric case. Transition is apparently initiated by a similar vortex ring/wall interaction reported by Sherwin and Blackburn. In the former, the geometric anomaly causes the position of the starting vortex to move towards the near wall via mutual induction, whereas for the latter it is the velocity perturbation that biases the position of the vortex ring.

Varghese (2006) used DNS data for symmetric and eccentric stenotic flows as a baseline for analysing and comparing the performance of various turbulence models. The turbulence models included standard two-equation models (e.g.  $k-\epsilon$  and  $k-\omega$ ) as well as more advanced Reynolds stress models. His results showed that all of these standard turbulence models performed poorly, each predicting an immediate transition to turbulence at the stenosis.

*In vivo*, the skewed axial velocity profile is observed downstream of a bifurcation, while secondary flows are induced by curvature. In tandem, these two disturbances are characteristic of flow downstream of a bend. The focus of this study was to determine the impact of inlet conditions on the flow development distal to an idealized stenosis under physiological forcing. Experimentally obtained data were used to understand the influence of the axial velocity profile and secondary flows on the stenotic flow, and to establish the consequent implications on numerical modelling.

## 2. Experimental setup

A schematic diagram of the two experimental configurations used in these experiments is shown in figure 1. The flow loop in both configurations is driven by an Ismatec programmable gear pump with a magnetically coupled Micropump A-mount cavity style pump head. The flow loops can be operated in either a steady or pulsatile flow mode. The steady and pulsatile flow paths are differentiated in figure 1 by dashed and solid arrows, respectively. In pulsatile mode, the mode used in all experiments discussed herein, the flow is driven directly by the pump. The flow loop in figure 7(*a*) is used for the baseline and linear insert cases, while the flow loop in figure 7(*b*) is used in the bend case. The coordinate systems shown in the two subfigures indicate that  $x$  is the streamwise coordinate in the test section (downstream of the stenosis), while  $y$  and  $z$  are the radial coordinates. The locations of the two coordinate systems are not meant to imply the origin. In all stenotic flow experiments the origin is at the throat of the stenosis along the centreline of the tube.

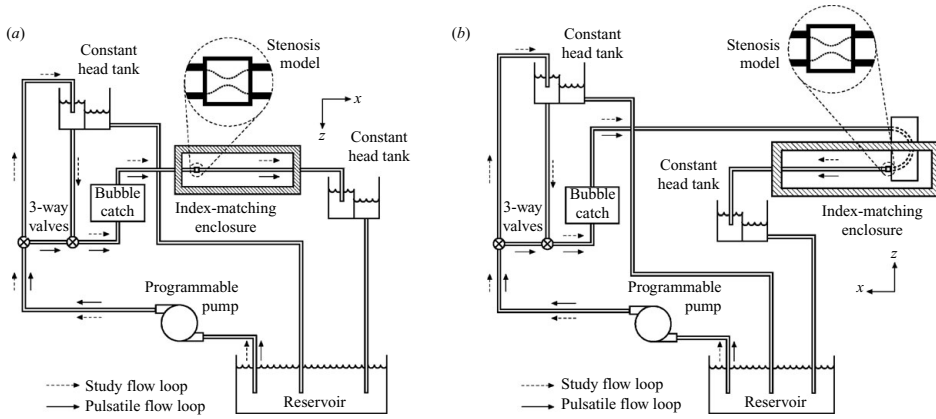


FIGURE 1. Schematic diagram of experimental setups; (a) baseline and linear insert and (b) bend.

A 1.15 m long by 12.6 mm ID by 1.2 mm thick glass tube ( $L/D \sim 96$ ) upstream of the test section provides adequate development length to produce fully developed flow. Flow in the conditioning section is laminar with maximum Reynolds numbers ranging from 500 to 1500. In this range, the required steady flow entrance length is  $L_e/D = 0.06 Re_{\bar{v}}$ , where  $L_e$  is the entrance length and  $Re_{\bar{v}}$  is the Reynolds number based on average velocity and tube diameter. At low to moderate Womersley number ( $\alpha < 12.5$ ), the development length of pulsatile flow obeys the same Reynolds number relation as in steady flow, except that the Reynolds number is based on maximum centreline velocity for the unsteady flow Ku (1997). The entrance lengths corresponding to these Reynolds numbers range from 30 to 90 tube diameters. The fluid exits the test section into another constant-head tank to ensure a constant exit pressure. The exit tank has an overflow chamber that drains into the main reservoir, completing the flow loop. Alignment brackets in the index matching enclosure support the stenosis model, as well as the upstream and downstream tubing sections. The brackets minimize misalignment, which would result in asymmetry of the jet trajectory.

Glass was selected for the tubing material because of its optical clarity and tight dimensional tolerances from the manufacturer. Arterial vessels are naturally compliant, but this elasticity has been shown to have a secondary effect on the flow features Ku (1997). Furthermore, the arteries lose their compliance with age, with the elderly population experiencing a marked decrease in vessel distensibility. Bortolotto *et al.* (1999) found that by age 74, men with normal blood pressure have lost 43 % of their carotid artery distensibility in comparison with 35-year-old subjects. Because the elderly demographic is significantly impacted by cardiovascular disease, the rigid-tube model is justifiable as clinically relevant.

Following Ahmed & Giddens (1983), the stenosis geometry is generated by revolving an offset cosine curve about the symmetry axis ( $x$ -axis). The equations defining the stenosis geometry, from Varghese *et al.* (2007a), are

$$S(x) = \frac{D}{2} \left[ 1 - s_o \left( 1 + \cos \left( \frac{2\pi(x - x_o)}{L} \right) \right) \right], \quad (2.1)$$

$$y = S(x) \cos \theta, \quad (2.2)$$

$$z = S(x) \sin \theta, \quad (2.3)$$

where  $D$  is the unoccluded tube diameter,  $s_o$  is fraction of unoccluded area,  $L$  is the stenosis length, and  $x_o$  is the distance from the inception point of the stenosis to the throat. The ranges for  $x$  and  $\theta$  are  $0 \leq x \leq L$  and  $0 \leq \theta < \pi$ , respectively. The origin of coordinates for studies described herein coincide with  $x_o$  in (2.1). The stenosis model occludes 75% of the tube area (corresponding to a 50% reduction in diameter). The model was constructed using stereolithography. The stenosis was built along the  $x$ -axis. The model was designed such that the flow conditioning and test section tubes slide into either side of the stenosis and seal with an o-ring. The raw stenosis part was lightly sanded to reduce the ridges inherently produced in lithography without significantly changing the shape. The sanded model was sealed with urethane to prevent water absorption, which produced a smooth finish. Upon insertion into the flow loop the tube/stenosis interface was sealed using silicone caulk.

### 2.1. Waveform generation

The physiological waveform used in this study is that which is measured in the human common carotid artery. The predisposition of the carotid bifurcation to atherogenesis has prompted several researchers to document the arterial geometry and volume flow waveform in the common carotid artery (see Bharadvaj, Mabon & Giddens 1982; Holdsworth *et al.* 1999; Hyun *et al.* 2000; Stroud *et al.* 2002). The waveform employed in this study is based upon pulsed-Doppler ultrasound measurements by Holdsworth *et al.* (1999) of the common carotid artery of 17 normal, healthy human subjects with no known atherosclerotic lesions. They constructed an archetypal waveform based upon ‘feature points’ identified in the measured waveforms. Their prototypical waveform (figure 11 in their paper) was digitized using *Engauge* digitizing software and interpolated to a uniform time axis using a cubic spline fit. The mean, minimum and maximum Reynolds numbers were computed from the respective volumetric flow rates provided in their table 4 for the prototypical waveform. The Reynolds numbers were calculated assuming the viscosity and density of blood to be 3.5 cP and  $1060 \text{ kg m}^{-3}$ , respectively, and the diameter of the common carotid artery to be 6.4 mm. This is the diameter measured by Holdsworth *et al.* (1999) and is in agreement with prior measurements. They measured the average period to be 0.917 s, although they noted a fair degree of variability from subject to subject. This period is similar to that reported by Bharadvaj *et al.* (1982) and approximately 30% larger than the value used by Stroud *et al.* (2002). The Womersley and Reynolds numbers computed from Holdsworth’s data are presented in table 1. Their *in vivo* waveform was scaled to the present experiment by matching the Reynolds and Womersley numbers. Using the density and viscosity of water ( $1000 \text{ kg m}^{-3}$  and 1.0 cP, respectively), matching Womersley numbers required the period be scaled up to 11.55 s. The flow rate was scaled to match the Reynolds number. Included in table 1 are the reduced velocity and peak-to-mean flow ratios defined by Sherwin & Blackburn with values of 26.3 and 3.9, respectively. The present values are considerably greater than the ranges  $2.5 \leq U_{\text{red}} \leq 7.5$  and  $U_{\text{pm}} = 1.75$  considered by Sherwin & Blackburn.

The quality of the pump output was found to depend on the smoothness of the input voltage. Mitigation of Gibb’s type ringing at the peaks was accomplished by decomposing Holdsworth’s waveform into Fourier modes and reconstructing a version of the original waveform using a small number of modes. A 10-mode Fourier reconstruction was found to capture the essence of the waveform while eliminating the higher frequencies, which caused oscillations in the pump. The Fourier coefficients of the scaled-up waveform are presented in table 2. The Fourier-reconstructed waveform is shown in figure 2.

Mean velocity, $\bar{u} = 4Q_{\text{avg}}/(\pi D^2)$	2.87 cm s <sup>-1</sup>
Mean Reynolds number, $Re_{\text{avg}} = 4Q_{\text{avg}}/(\pi \nu D)$	364
Minimum Reynolds number, $4Re_{\text{min}} = Q_{\text{min}}/(\pi \nu D)$	24
Maximum Reynolds number, $4Re_{\text{max}} = Q_{\text{max}}/(\pi \nu D)$	1424
Womersley number, $\alpha = D/2\sqrt{\omega/\nu}$	4.6
Reduced velocity, $U_{\text{red}} = \bar{u}T/D$	26.3
Peak-to-mean velocity ratio, $Re_{\text{max}}/Re_{\text{avg}}$	3.9

TABLE 1. Dimensionless parameters governing the bulk flow.

1.00000 + 0.00000i
0.10654 - 0.24469i
-0.16112 - 0.28013i
-0.24915 + 0.11904i
-0.08746 + 0.11309i
0.09169 + 0.19347i
0.11648 - 0.04419i
0.00544 - 0.04634i
-0.01204 - 0.02023i
-0.01768 + 0.00698i
0.00362 + 0.01425i

TABLE 2. Fourier coefficients used to construct the scaled-up smooth pump input waveform normalized by  $Q_{\text{avg}} = 3.57943 \text{ ml s}^{-1}$ .

Figure 3 compares the experimentally measured velocity profile time-trace to the theoretical Womersley solution for the Fourier-reconstructed waveform in the fully developed upstream tube section. The axes in the two subfigures correspond to non-dimensional radial position  $z/D$ , time  $t/T$  and mean streamwise velocity  $u/u_c$  (see §2.2.3 for the definition of  $u_c$ ). Thus, figure 3 represents the temporal evolution of the velocity profile at one axial position in the upstream flow development region. The input waveform is shown in an inset in figure 3(a), and the three prominent pulses of the waveform are labelled ‘primary’, ‘secondary’ and ‘tertiary’ in figure 3(b). Reversed flow near the walls occurs immediately after the deceleration phase of the primary pulse and in the valley between the secondary and tertiary pulses. Qualitatively, the two subfigures are in very good agreement, suggesting that the flow is fully developed and reasonably approximates the assumptions of the Womersley solution. Direct comparison of the experimental profiles with the analytical solution is shown in figure 4. The comparison shows good agreement between experiment and theory. The largest deviation occurs near the peak of the cycle, which was found to be the most difficult portion of the waveform to match. There is a slight phase lag between the experimental data and the analytical solution because of the phase lag between the pressure and velocity waveforms in Womersley flow. Further comparison between experiment and theory is provided in figure 5(a), which shows good agreement between experimental and theoretical velocity profiles at a few distinct phases. Figure 5(b) shows the streamwise root mean square (r.m.s.) velocity fluctuations at the same phases. The r.m.s. velocity fluctuation is approximately 2% for the majority of the cycle, the exception being during the maximum velocity ( $t/T = 0.167$  on the plot) when it rises to 4%. A distinct two-peak shape in the r.m.s. velocity profile observed by Beratlis *et al.* (2005) was not observed and the measured velocity fluctuations appear to be due to the measurement

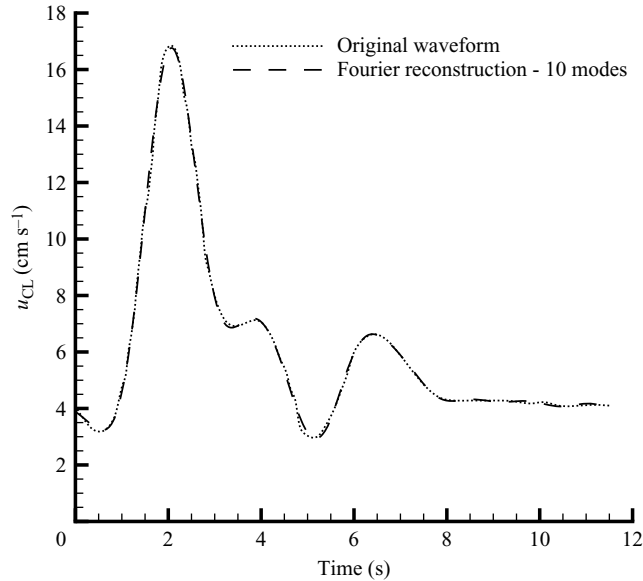


FIGURE 2. Comparison between the scaled-up waveform obtained by digitizing figure 11 in Holdsworth *et al.* (1999) and a reconstruction of that waveform using the first 10 Fourier coefficients.

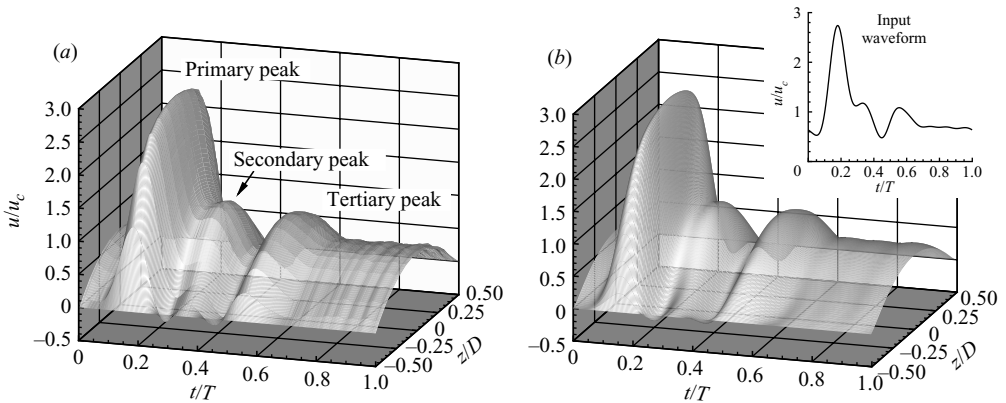


FIGURE 3. Fully developed pulsatile pipe flow velocity profile time-trace; (a) experimental data, (b) Womersley solution.

system and background noise only (similar magnitudes were observed in steady flow experiments).

## 2.2. Experimental techniques

Data were collected using laser Doppler velocimetry (LDV) and particle image velocimetry (PIV). A brief summary of the experimental techniques and estimates of experimental uncertainties are given below.

### 2.2.1. LDV system details

LDV is a minimally invasive, point velocity measurement technique capable of yielding up to three unambiguous velocity components with high temporal and spatial resolution (Adrian 1996). A commercial one-component LDV system (Dantec

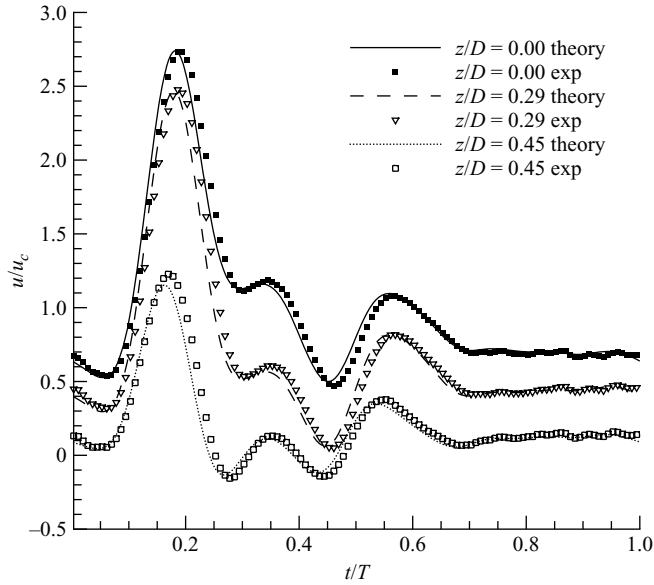


FIGURE 4. Fully developed pulsatile pipe flow velocity time-trace at various spanwise locations; comparison between experiment and theory.

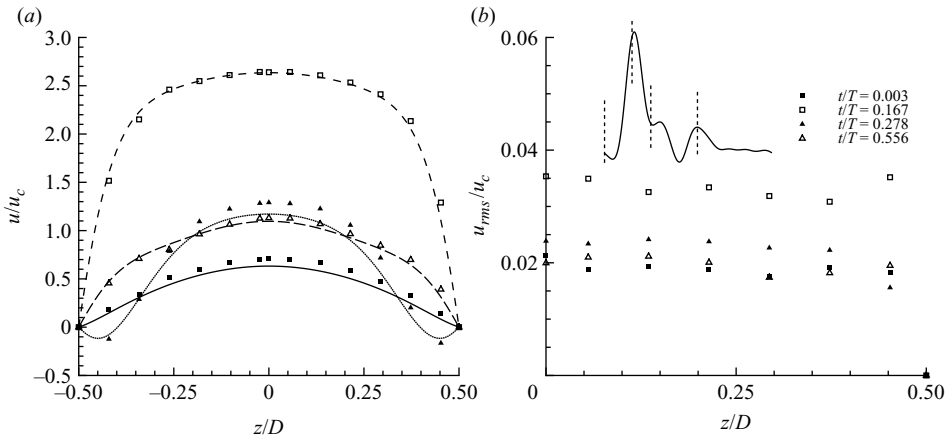


FIGURE 5. Fully developed pulsatile pipe flow velocity profile at various phases; symbols are experimental data, lines are theoretical predictions; (a) mean velocity, (b) r.m.s. velocity fluctuations.

Dynamics *FlowLite*) operating in burst mode was used in this study. A helium–neon laser produced a 632.8 nm beam that was split by a Bragg cell. The Bragg cell shifted the frequency of the beams by  $\nu_s = 40$  MHz with respect to one another. The LDV head lens had a focal length of  $f = 160$  mm and the beams were separated by 38 mm at the lens exit pupil. The manufacturer-specified divergence angle of the beams was  $2\kappa_o = 13.54^\circ$  in air. As the working fluid was water, refraction caused the actual beam divergence angle at the measurement location to be  $10.17^\circ$ . The beam diameter was nominally 1.35 mm and reduced down to  $\approx 0.1$  mm at its focal point. The beam waist value is only an approximation due to the effect of the index-matching enclosure on

the true focal length. The spatial resolutions were approximately 0.1 mm by 0.1 mm by 1.0 mm.

The fringe spacing in the measurement volume was 2.683  $\mu\text{m}$ . The fringe spacing did not change as a result of the change in index of refraction as both the beam divergence angle and the beam wavelength change by the same factor. Thus, the unadjusted values of  $\kappa$  and  $\lambda$  may be used to compute the fringe spacing. From the Bragg cell frequency, the anticipated fringe velocity can be computed,  $u_f = 107.32 \text{ m s}^{-1}$  (Adrian 1996). This is the velocity that should be measured for a particle at rest within the measurement volume. This value was confirmed by placing a 3  $\mu\text{m}$  hair in the measurement volume and recording the velocity. The measured and computed fringe velocities were identical to within four significant digits.

All signal processing was performed using the Dantec Dynamics BSA Flow Processing software. Down-mixing of the Bragg cell frequency (conversion of the typical 40 MHz frequency to lower frequencies) was performed automatically to facilitate the low-velocity measurements in these experiments. Additional flow seeding beyond the naturally occurring water particulates was not required, but 18  $\mu\text{m}$  diameter silvered hollow glass spheres were added to increase the data rate. The sample rate was approximately 200–1000 Hz, with the highest values occurring near the tube centreline and the lower near the tube walls. Data were collected for 100 cycles, leading to an average of approximately 350 000 data points per data set. For averaging, the data were binned into 720 bins.

The probe was attached to a two-direction manual traverse consisting of two lead screws, each controlling one coordinate direction. Vernier calipers attached to the traverse provided positioning data accurate to within  $\pm 0.05 \text{ mm}$ .

The uncertainty in the LDV measurements was approximated by obtaining velocity profiles along the jet centreline in two orthogonal directions under steady Poiseuille flow conditions and comparing the measured values to the theoretical parabolic profile. Velocity profiles were obtained in the  $y$  and  $z$  planes. Two profiles were obtained in each of the two directions. The mass flow rate was measured using the bucket and stopwatch method to be  $\dot{m} = 10.65 \pm 0.024 \text{ g s}^{-1}$ . The magnitude of  $u_{\text{max}}$  was  $17.06 \pm 0.143 \text{ cm s}^{-1}$ . The water temperature during the experiment was a constant 23.8°C and the corresponding density of 0.9982  $\text{g cm}^{-3}$  was considered constant in the uncertainty calculation. The Reynolds number of the flow was  $Re_{\bar{v}} = 1075$ . Far from the walls the error was approximately  $\pm 1\%$  and increased to  $\pm 5\%$  in the vicinity of the tube walls.

### 2.2.2. PIV system details

Over the past decade PIV has become a standard tool of experimental fluid mechanics (Raffel, Willert & Kompenhans 1998). Traditional PIV is an instantaneous planar velocity measurement technique adapted from speckle metrology in solid mechanics. PIV is conceptually simple; the velocities of small tracer particles within a specified plane in the fluid are determined by measuring their displacement over a short time.

All PIV experiments described herein were performed with a commercial TSI PIV system. The system consisted of a 2000  $\times$  2000 pixel PowerView 4MP camera, a dual 50 mJ pulse<sup>-1</sup> NewWave Gemini Nd:YAG laser, a TSI synchronizer and a dual Pentium III data acquisition computer. TSI's Insight 3G software was used to correlate the images. The images were correlated using a multipass FFT scheme with continuous window shifting, a Gaussian subpixel interpolation scheme and a central difference algorithm for velocity computation. The interrogation regions ranged from

$32 \times 32$  to  $64 \times 64$  pixels and  $\Delta t$  was typically between 250 and 800  $\mu\text{s}$ . Each pixel corresponded to  $15 \mu\text{m}$  in the image plane resulting in a spatial resolution on the order of  $0.25 \text{ mm}^2$  for the twice oversampled data (i.e. the interrogation windows were overlapped by 50%). The pixel size in the image plane was determined by measuring the outside diameter of the tube with calipers and combining this with the size (in pixels) of the image of the tube. This measurement was performed 10 times and the results were averaged. The PIV system was phase-locked to the pump via a custom-designed pump-controller LabView VI. One hundred image pairs were used to compute the average vector fields.

Data from the PIV uncertainty experiments were obtained in the  $x$ - $z$  plane. The Reynolds number based on average velocity was 705 and the mass flow rate was  $6.98 \pm 0.02 \text{ g s}^{-1}$  for these experiments. This corresponds to average and centreline velocities of  $5.58 \pm 0.05 \text{ cm s}^{-1}$  and  $11.17 \pm 0.09 \text{ cm s}^{-1}$ , respectively. The average velocity field was obtained by averaging 2000 instantaneous PIV realizations interrogated using a multi-pass scheme. The data were first computed using a  $64 \times 64$  pixel interrogation region followed by pass validation. The displacement results were used to shift the centre of the interrogation region in the second pass, which used a  $32 \times 32$  pixel region. The final vector field was validated using range and standard deviation statistics. No interpolation was used on the final vectors. Due to the removal of spurious vectors in the validation scheme, each vector in the mean velocity field represented an average of 1000–1400 instantaneous realizations.

Over the majority of the profile the error in the mean velocity is less than  $\pm 3\%$ . Near the wall the error increases to approximately  $\pm 5\%$ . In the very near wall region the relative error becomes very large ( $>40\%$ ), due in part to distortion from the cylinder.

### 2.2.3. Normalization schemes

Two averaging schemes are employed in this study; these are average centreline normalization and inlet velocity waveform (IWF) normalization. The average centreline velocity normalization divides the velocity by that at the centreline of the tube upstream of the stenosis,  $u_c$ , where

$$u_c = \frac{1}{T} \int_0^T u_{cl}(t) dt. \quad (2.4)$$

The numerical value of  $u_c$  for the applied waveform is  $6.1 \text{ cm s}^{-1}$ . IWF normalization consists of normalizing the velocity at each phase of the waveform by the corresponding upstream centreline velocity at that phase. This is symbolized by  $u_{iwf}$ ;

$$u_{iwf,k} = \frac{\left( \frac{1}{N_k} \sum_{n=1}^{N_k} u_n \right)_k}{\left( \frac{1}{M_k} \sum_{m=1}^{M_k} u_{c,m} \right)_k}, \quad (2.5)$$

where the subscript  $k$  denotes the phase (bin) being averaged,  $N_k$  and  $M_k$  correspond to the number of velocity measurements in that particular bin,  $u_n$  is the  $n$ th measured velocity at a given phase bin, and  $u_{c,m}$  is the  $m$ th measured velocity at the corresponding phase of the upstream flow.

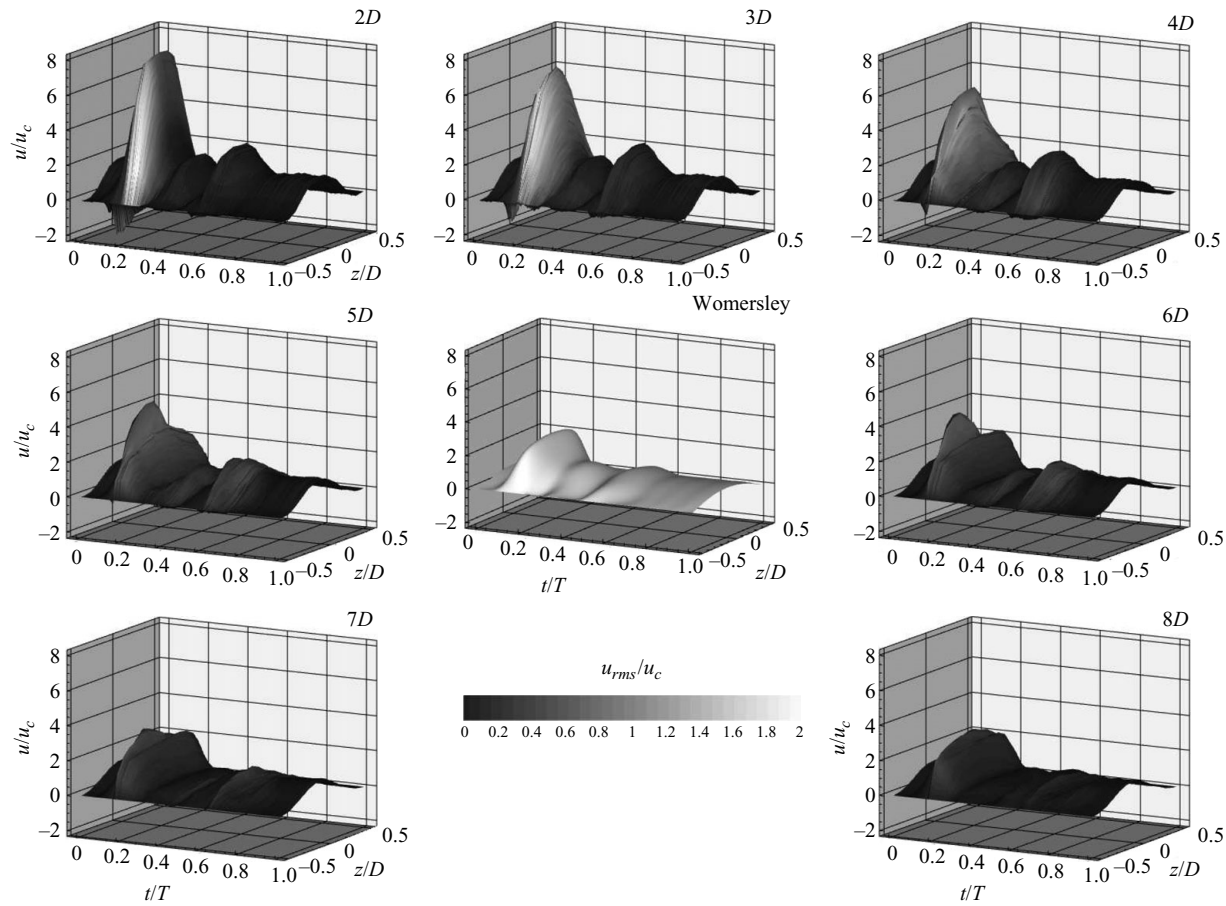


FIGURE 6. Velocity profile evolution between  $2D$  and  $8D$  downstream of the stenosis. Contours of r.m.s. velocity fluctuations overlaid.

### 3. Baseline flow results

Ojha *et al.* (1989) identified four flow-regime zones downstream of an idealized stenotic flow. The four zones are an initial stable jet in the near field ( $z/D < 3$ ), a transition region ( $3.5 \leq z/D < 4.5$ ), a turbulent region ( $4.5 \leq z/D < 7.5$ ), and a relaminarization region ( $z/D \geq 7.5$ ). Mean velocity profiles at each position downstream of the stenosis from  $x/D = 2$  to  $x/D = 8$ , presented in figure 6, qualitatively agree with these regimes. At  $x/D = 2$  the stenotic jet is well defined and the r.m.s. velocity fluctuations (the contour overlaid on the velocity profiles) are small, except in the shear layer. The jet associated with the primary waveform peak is blunt and plug-like, as expected, because of the strong acceleration through the stenosis.

At  $x/D = 3$  the sharply defined stenotic jet resulting from the primary waveform peak has eroded some and the r.m.s. velocity fluctuations along the tube centreline have increased (the fluctuating velocity in the shear layer has decreased a bit). This is the region between the stable jet of zone I and the transition region of zone II. At  $x/D = 4$  to 6 the magnitude of the primary stenotic jet (i.e. the jet produced by the primary pulse) has decreased in magnitude and spread out radially. The spreading of the mean jet is in part due to unsteadiness in the jet location as shown by the PIV data in a subsequent section. In this region the r.m.s. velocity associated with the tertiary pulse has increased as that jet breaks down. By 8 diameters downstream of the stenosis throat the velocity profile character resembles the analytical solution. The r.m.s. velocity fluctuations are small and the flow has entered the relaminarization stage.

The phase-averaged centreline velocity as a function of distance downstream and time is presented in figure 7. The axes correspond to the axial distance downstream of the stenosis,  $x/D$ , from 2 to 20, and phase of the cardiac cycle,  $t/T$ . The contours in figure 7(a) represent streamwise velocity magnitude and those for figure 7(b) are the r.m.s. velocity fluctuations. Superimposed on these plots (at  $x/D = 15$ ) is the input waveform for reference. Note the time axis is increasing from top to bottom. In the near field the stenotic jet discussed in reference to figure 6 is indicated by dark contours. The velocity drops precipitously downstream of  $6D$  due to stenotic jet breakdown. Flow redevelopment occurs throughout the remainder of the test section. As labelled on the figure, a temporal shift in the peak velocity location (with respect to the input waveform) occurs between  $2D$  and  $6D$  for each peak. As discussed later, the peak shift is a manifestation of the jet formed at the throat and the associated vortex ring at the front of the jet. The r.m.s. velocity fluctuations (figure 7b) reach a maximum between  $3D$  and  $5D$  for the primary peak, while the largest fluctuations in the secondary and tertiary peaks occur between  $5D$  and  $7D$ . These are the regions in which the velocity drops rapidly, a manifestation of the stenotic jet and vortex ring breakdown.

A direct comparison of centreline velocity at select spatial locations is presented in figure 8. The velocity waveform upstream of the stenosis is represented by square symbols. The maximum velocity at  $x/D = 2$  is nearly three times that of the upstream flow. By  $6D$  the velocity is not appreciably larger than the upstream velocity, but there are obvious spikes at the primary and tertiary peak phases. Furthermore, it is obvious that the primary and tertiary peaks are propagating downstream (particularly the tertiary peak). The relaxation portion of the waveform  $t/T > 0.8$  is characterized by markedly higher velocities up to  $\sim 7D$ . The velocity profiles at  $8D$  and  $10D$  are nearly identical with lower magnitudes than the upstream velocity. At  $15D$  the velocity magnitude is slowly approaching the fully developed condition.

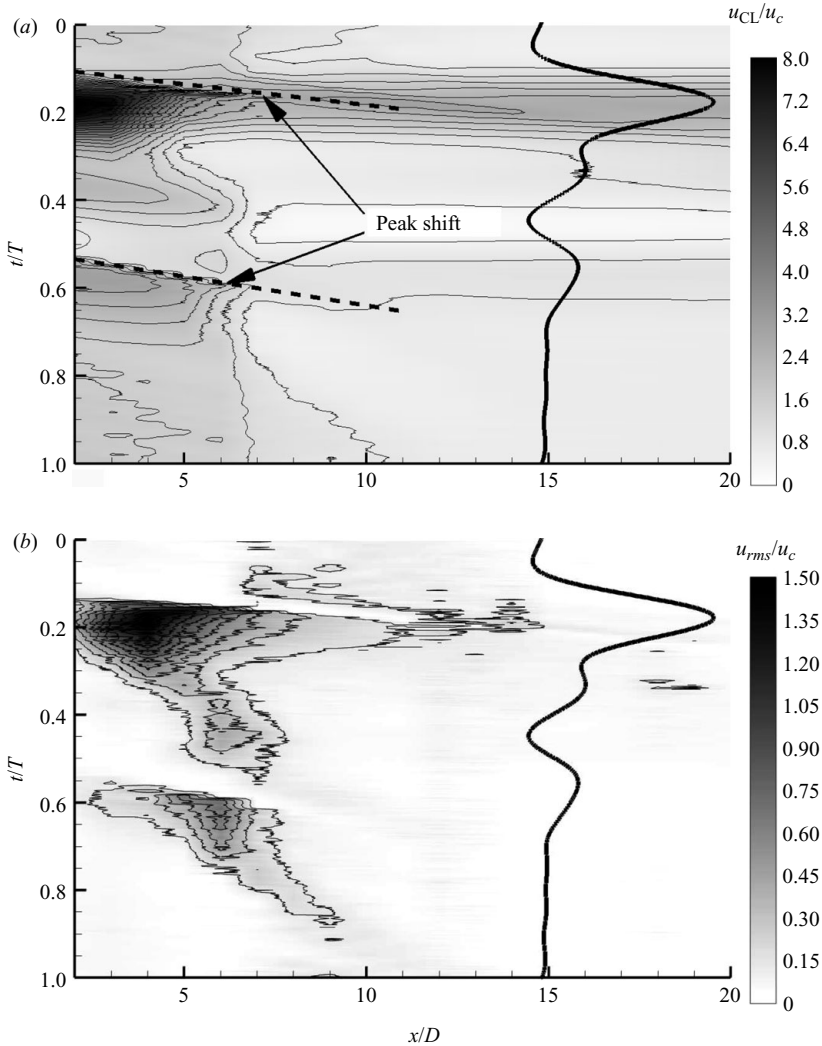


FIGURE 7. Contour plot of centreline velocity versus time; baseline case (a) velocity magnitude, (b) r.m.s. velocity fluctuations.

PIV data in figure 9 show the propagation of the coherent tertiary vortex ring up to  $x/D = 4$ . The vortex core is identified using the two-dimensional  $Q$ -criterion developed by Weiss (1991). The line contour represents a numerical value of  $Q = -200$ . These data are instantaneous velocity fields obtained during different pulse cycles and do not represent the propagation of a single-vortex ring. The low frame rate of the camera precluded time-resolved PIV results. Consequently, direct measurement of the vortex ring velocity was not possible. At  $t/T = 0.54$ , a vortex ring is located at  $x/D \approx 2.1$ , as marked by an arrow on the abscissa. This correlates well with the phase and location of the 'peak shift' observed in figure 7. The leading vortex ring is located at  $x/D \approx 2.6$  at  $t/T = 0.55$ ,  $x/D \approx 3.2$  and  $t/T = 0.56$  and  $x/D \approx 4.9$  at  $t/T = 0.57$ . Vortices upstream of the leading vortex are likely to produce other rings by the shear layer instability.

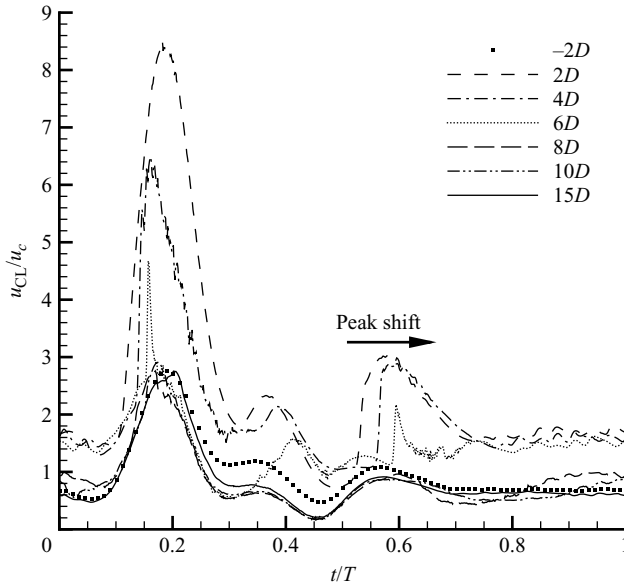


FIGURE 8. Comparison of centreline velocity waveforms from  $2 \leq x/D \leq 15$ .

The slope of the lines connecting the leading edge of the primary and tertiary pulses (labelled as ‘peak shifts’ in the  $x-t$  space of figure 7) indicate that the primary vortex ring (and subsequent stenotic jet) propagates at a higher velocity than the tertiary ring. The slope of each line is nearly constant, consistent with the observations of Sherwin & Blackburn (2005) that vortex rings in pulsatile flow propagate at nearly constant velocity despite large variations in the bulk-flow velocity. The arrival of the stenotic jet/vortex ring results in a rapid increase in velocity at a specified centreline position. The first derivative,  $(u_{i_{wf,k+1}} - u_{i_{wf,k}})/\delta t$ , found in figure 10, can be used to locate the phase which the pulse arrives at a particular measurement location. The rapid increase in velocity is represented by a clear spike in the acceleration waveform. The spikes associated with the primary and tertiary pulse at measurement locations from  $x/D = 2$  to 6 are expanded in the insets. The approximate propagation velocity of the primary and tertiary peaks, obtained from the time difference between successive spikes, is  $10.9$  and  $7.3 \text{ cm s}^{-1}$ , respectively.

Despite the lack of temporal resolution in the PIV data, it is nonetheless possible to estimate the ratio of primary to tertiary vortex ring velocity by recognizing that ring velocity is proportional to  $\Gamma/R$ , where  $\Gamma$  is the circulation and  $R$  is its radius. The average circulation of the primary vortex ring at inception was computed by performing the line integral along a rectangle encompassing the vortex centre. The average primary and tertiary vortex ring circulations computed from this method are  $\sim 4.5$  and  $\sim 2.8 \text{ cm}^{-2} \text{ s}^{-1}$ , respectively. The standard deviation of both circulation measurements is approximately 20%. The ring Reynolds numbers, defined as  $\Gamma/\nu$ , are 450 and 280, respectively. This Reynolds number range is well within the laminar vortex ring regime. The average ring radius for the primary and tertiary ring is  $0.41D$  and  $0.43D$ , respectively. The standard deviations are 5% and 3%, respectively. The ring radius was computed by measuring the distance between the centres of the vortex pairs (the cross-section of the ring) in each instantaneous image and dividing by two. Thus, tilted vortex rings have a larger radius. It is assumed that the PIV image bisects

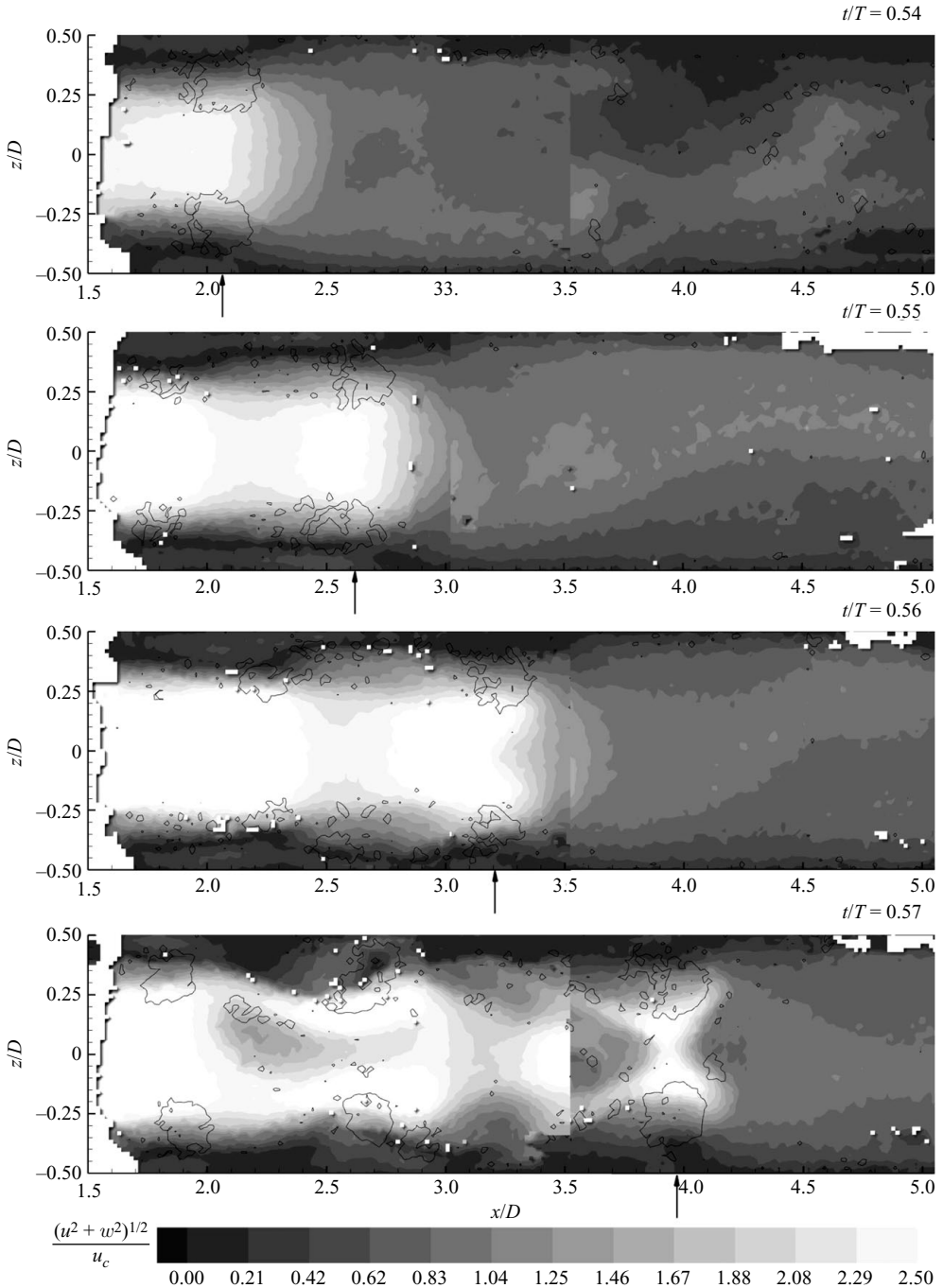


FIGURE 9. Vortex ring propagation initiating at the tertiary peak. Flood contour is velocity magnitude and the lines are the  $Q$ -criterion showing the vortex cores. Arrows at the bottom signify the vortex ring location. Other vortices are shear layer vortices or trailing vortex rings.

the ring through the centre point, which may not be the case for each individual ring. The ratio of the velocities computed from  $(\Gamma/R)_{\text{primary}}/(\Gamma/R)_{\text{tertiary}}$  is 1.68. The ratio of velocities computed from the mean centreline LDV data (figure 10) is 1.50. These

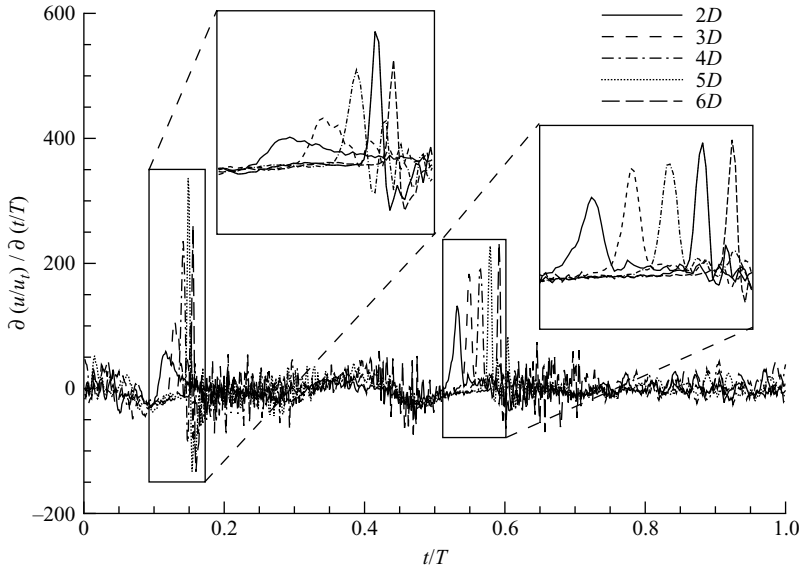


FIGURE 10. Acceleration at several locations distal to the stenosis to highlight peak shifting; baseline case.

---

Primary pulse	
Circulation, $\Gamma/(u_c D)$	0.58
Radius, $R/D$	0.41
Reynolds number, $\Gamma/\nu$	450
Tertiary pulse	
Circulation, $\Gamma/(u_c D)$	0.36
Radius, $R/D$	0.43
Reynolds number, $\Gamma/\nu$	280

---

TABLE 3. Vortex ring parameters for the baseline flow case.

independent estimates of propagation speed are in reasonable agreement, particularly considering the large uncertainty in these calculations. This supports the assertion that the peak shift observed in the LDV data is the signature of vortex ring propagation. These results are summarized in table 3.

Blackburn & Sherwin (2007), in an extension to their previous stenotic flow stability studies, used a Floquet analysis to determine two-vortex ring instability mechanisms. At reduced velocities less than 2 they found a wavy core instability mode, similar to the Widnall instability identified for free vortex rings. At higher reduced velocities they had previously found (Sherwin & Blackburn 2005) a tilting mechanism. In the present study,  $U_{\text{red}} \approx 27$ , which is well above the threshold where the Widnall-type instability is dominant, so the instability would be expected to be of the vortex-tilting type in preference to the Widnall type. Using a combination of DNS results and the Floquet analysis, Blackburn & Sherwin developed a neutral stability curve for both instability modes and found that for  $U_{\text{red}} > 5$  the critical Reynolds number increases nearly linearly. By digitizing the curve in their figure 23 and fitting a

line to the data for  $U_{\text{red}} > 6$  and extrapolating that line to the current reduced velocity yields a critical Reynolds number of  $\simeq 1180$  (assuming that the linear trend persists as the reduced velocity increases). The Reynolds number in the present study (based on average velocity) is greater than this critical value only in the range  $0.15 \leq t/T \leq 0.20$ , and the Reynolds number based on  $u_c$  is only 384. We also have multiple harmonics in the waveform, which Sherwin & Blackburn (2005) found to have a stabilizing effect. Thus, it is questionable whether the vortex-tilting instability plays an active role in the breakdown mechanism in the present study. Blackburn & Sherwin (2007) found the convective shear layer instability to play a very prominent role for high reduced velocities, in that it acts as a destabilizing mechanism for the vortex-tilting instability. For  $U_{\text{red}} = 10$  they found the convective instability to be large enough that it obscured the period-doubling instability in their DNS results. By superposing a small amplitude harmonic streamwise perturbation on the mean flow, Blackburn & Sherwin found that the convective shear layer instability sensitivity increased with increasing reduced velocity. As the reduced velocity increased, however, so did the Reynolds number, so it cannot be clearly determined whether the increased sensitivity results from the increase in reduced velocity, the increase in Reynolds number, or some combination thereof. In the present study, the reduced velocity ( $U_{\text{red}} = 27$ ) is considerably higher than any case considered by Blackburn & Sherwin, but the Reynolds number is generally lower. Consequently, it is difficult to infer whether the convective shear layer instability plays a similar role in the present experiments. Furthermore, there is a relatively high level of noise in the experiment (in comparison with the noise levels in numerical simulations) and geometric imperfections that can also break symmetry. Therefore, while it is very likely that the convective shear layer instability plays a role, and may induce the vortex-tilting instability mechanism, despite the relatively low Reynolds number, the degree to which these mechanisms influence the stenotic jet/vortex ring breakdown cannot be determined.

### 3.1. Flow redevelopment

Figure 11 is a surface plot of the IWF normalized centreline velocity versus distance downstream and time. If the fully developed upstream waveform were recovered sufficiently far downstream of the stenosis, the IWF normalized velocity would be equal to 1 at all phases. However, the deviations of the far downstream centreline waveform from the input waveform are clear. In particular, a ‘ridge’ originating from the inception of the primary peak (labelled on the figure) is observed to advect through the entire domain. By  $20D$ , the ridge initiated during systole (i.e. the primary peak) and a ‘deficit’ at  $t/T = 0.45$  (also labelled on the figure) are the only significant deviations from the input waveform. The deficit does not advect downstream, but rather remains at the same phase, corresponding to the local minimum between the secondary and tertiary peaks of the input wave. A propagating ridge originating from the tertiary peak is also evident, but it is more disperse and dies out by approximately  $14D$ . As pointed out by Brasseur (1979), more energetic vortex rings are less impacted by the presence of the tube wall, which explains why the primary vortex ring propagates beyond the tertiary ring.

Brasseur developed a kinematic theory of vortex motion in a tube by superposing the velocity field of a free-vortex ring and the velocity imposed by the wall on the vortex ring. The theory is analogous to the two-dimensional case of a vortex pair propagating in a channel. The vortex pair propagates via mutual induction, while image vortices, used to enforce the no-penetration boundary condition at the wall, act

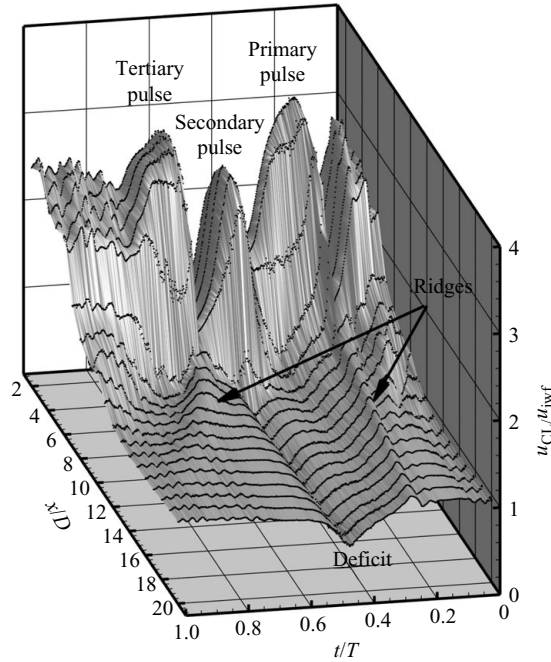


FIGURE 11. Contour plot of the IWF normalized centreline velocity versus time; baseline case.

to decelerate the pair. Therefore, Brasseur's statement is essentially that for a given vortex ring radius, the ring with greater circulation will advect faster, and thus be less influenced by the wall. The propagation speed of the disturbance that produces the ridge decreases slightly with distance downstream, although the change is small. It is unlikely that a coherent vortex ring can propagate so far downstream, but some disturbance does continue to propagate. Khalifa & Giddens (1981) reported a 'starting structure' as far downstream as  $x/D = 20$  for a 50% occlusion and to  $3.7 < x/D < 7.7$  for a 75% stenosis. Their reduced velocity was 18, corresponding to a critical Reynolds number of 850 (extrapolated from Blackburn & Sherwin 2007). Their Reynolds number was 950, so the vortex tilting instability should have been present.

Examples of the fluctuating velocity time-traces are presented in figure 12 from  $x/D = 2$  to 10. The driving mean velocity and acceleration waveforms are included at the bottom of the figure. Vertical lines are extended from the local maxima and minima of the forcing velocity (solid lines) and acceleration (dashed lines) waveforms throughout the figure for reference. Oscillations are initiated just after the primary peak of the acceleration waveform, prior to deceleration in the range  $2 \leq x/D \leq 6$ . At  $2D$ , the oscillations are smooth and their frequency varies with bulk flow speed. At the peak velocity of the primary pulse the frequency is highest and it tapers off at lower bulk speeds. This is suggestive of shear layer roll-up. Multiple vortices were observed in the PIV data (e.g. figure 9), in agreement with the velocity time-traces. The arrival of the stenotic jet and associated vortex ring is clearly observed up to  $x/D = 6$  by the shift in time of the 'burst' in the time-traces. Note that while a coherent ring was observed as far downstream as  $4D$  in the PIV data (and shear layer vortices

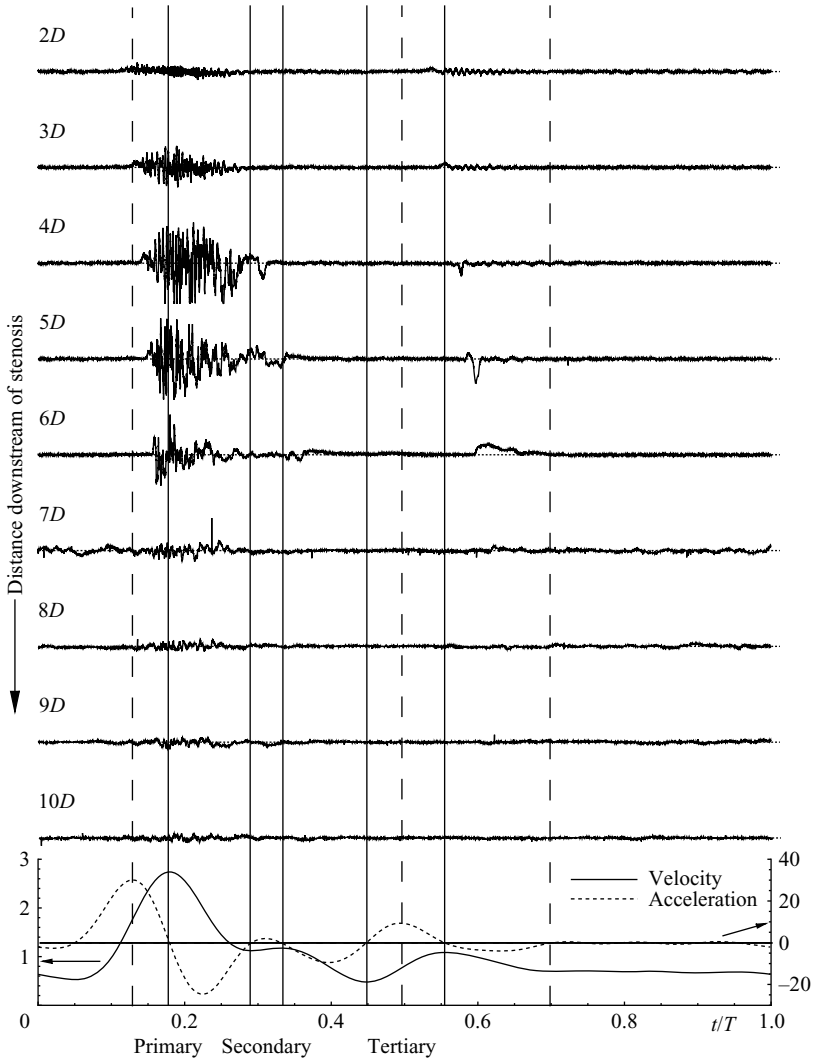


FIGURE 12. Comparison of representative fluctuating velocity time-traces at the tube centreline; baseline case.

were observed up to at least  $5D$ ), beyond those locations the bulk stenotic jet may no longer have an associated vortex ring.

The oscillations become severe and of higher frequency further downstream during deceleration of the bulk flow ( $0.18 \leq t/T \leq 0.28$ ). The oscillations are damped considerably by the time the acceleration corresponding to the secondary pulse becomes positive. It appears that stabilization of the fluctuations is also tied to the acceleration waveform, as damping seems to begin after the derivative of the acceleration changes sign. The velocity fluctuations associated with the tertiary pulse are minor compared to those observed for the primary one, potentially due to the lower Reynolds number. At this phase ( $t/T > 0.5$ ) the velocity time-traces do not display the erratic behaviour exhibited during the primary pulse. The high-frequency events, particularly during the primary pulse imply turbulent breakdown of the stenotic jet (and potentially the associated vortex ring). Further downstream ( $7 \leq x/D \leq 10$ ) noise

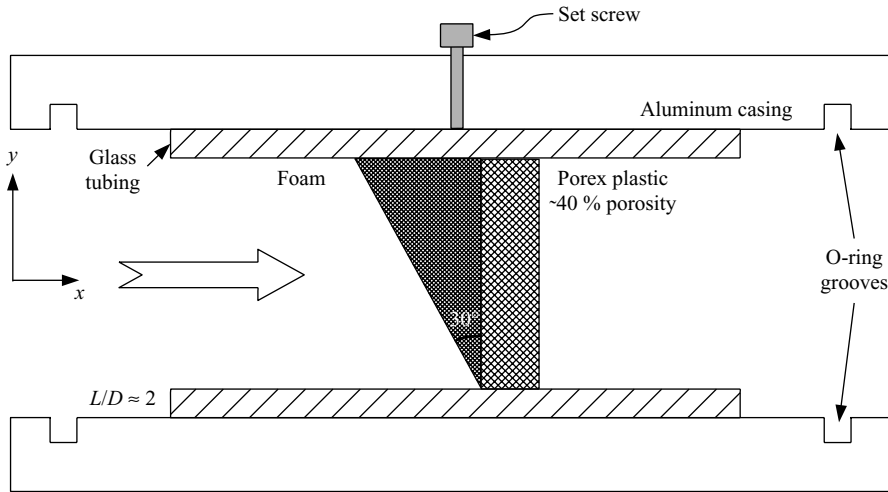


FIGURE 13. Schematic diagram of the insert used to induce an approximately linear mean velocity profile.

from the earlier breakdown of the stenotic jet is still observed during the primary pulse phases. For all locations, the flow is relatively steady between the secondary and tertiary peaks.

#### 4. Disturbances

This section presents the results from the two disturbed inlet cases investigated; skewed inlet profile and flow downstream of a bend. The flow field downstream of a bend has a skewed mean flow profile (peak velocity is biased away from the centreline), in addition to a secondary flow component (Dean's vortices). Details of how each disturbance was produced in the experiment precedes the results and discussion.

##### 4.1. Linear shear velocity profile disturbance

###### 4.1.1. Insert design

In an effort to decouple the effects of the mean flow profile from the secondary flow on the stenotic flow development, a shear flow-inducing insert is introduced, with the goal of skewing the location of maximum velocity away from the centreline.

The velocity gradient is produced by imposing a spatially varying resistance on the inlet flow via a porous insert. A schematic diagram of the porous insert is shown in figure 13. It consists of two layers. The first is a short cylinder of *Porex* plastic with porosity of approximately 40%. The *Porex* plastic is quite rigid and is press fitted into a short  $2D$  long piece of glass tubing. The *Porex* cylinder prevents the less rigid second layer from moving downstream during pulsation. The second layer is formed from standard packing foam for computer RAM. The foam is in the shape of an oblique cylinder, i.e. a cylinder that has been cut by a plane at an angle of  $30^\circ$  with respect to the  $r-\theta$  plane. The flow resistance imposed by the insert varies with the axial thickness, thus imposing a shear on the fluid downstream of the insert and producing a skewed velocity profile.

The glass insert is secured to the flow loop by an aluminum coupling, also shown in figure 13. The glass insert is held in place by a set screw. The upstream flow

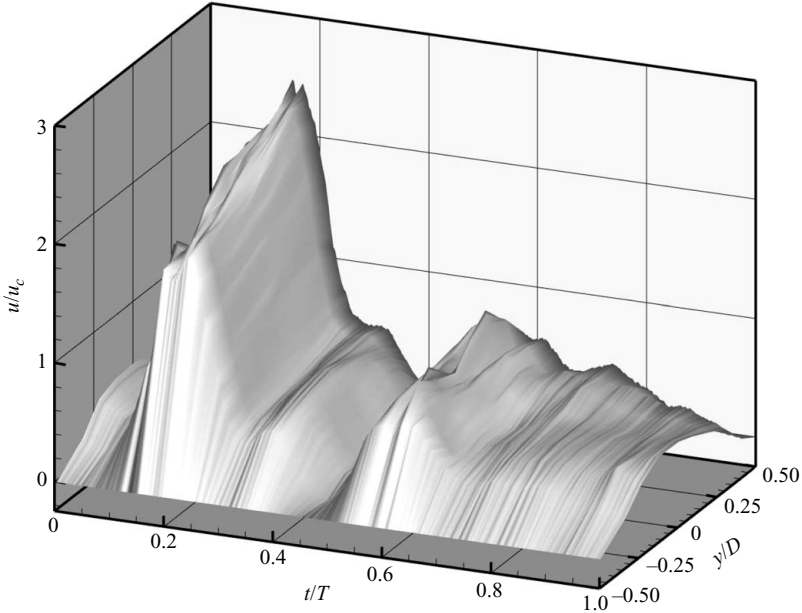


FIGURE 14. Velocity profile time-trace  $5D$  downstream of the shear insert.

conditioning section and the downstream test section are inserted in opposite ends and placed flush against the glass insert. O-ring grooves in the aluminum sleeve create a seal, which is reinforced by silicon placed on the outside of the casing. The linear insert was positioned  $5D$  upstream of the stenosis.

Figure 14 is a time-trace of the velocity profile  $5D$  downstream of the insert along the tube centreline (these data were collected without the stenosis in place and correspond to the location of the stenosis in the experiments). A nearly linear profile is apparent during the primary pulse, becoming less well defined during the low Reynolds number portions of the phase. The maximum velocity occurs at  $y/D \simeq 0.4$ , in contrast to  $y/D = 0$  for the baseline case (figure 3). A few selected velocity profiles are plotted in figure 15(a) to demonstrate their linearity. The data points have been connected by lines. Figure 15(b) shows the corresponding r.m.s. velocity fluctuations at each point, which increase with increasing Reynolds number. The normalized r.m.s. velocity fluctuations for the majority of the cycle are approximately 8% and increase to near 30% at the peak of the cycle. These r.m.s. velocities are considerably larger than those of the baseline case and are not uniform across the tube cross-section. The fluctuations are largest near the wall of the lower velocity ( $y/D < 0$ ) side of the insert. The inset in figure 15(b) shows the input waveform with vertical lines corresponding to the phases presented in the figure. Only negligible secondary flow downstream of the porous insert was measured, on the order of the uncertainty of the LDV measurements. This is more than an order of magnitude smaller than the secondary flow induced by the bend presented in §4.2. Therefore, the effects of the skewed velocity profile were isolated.

#### 4.1.2. Results

The mean centreline velocity resulting from the linear inlet velocity profile is compared with the baseline case for  $x/D \leq 10$  in figure 16. The skewed input profile forces a more rapid breakdown of the stenotic jet associated with the primary

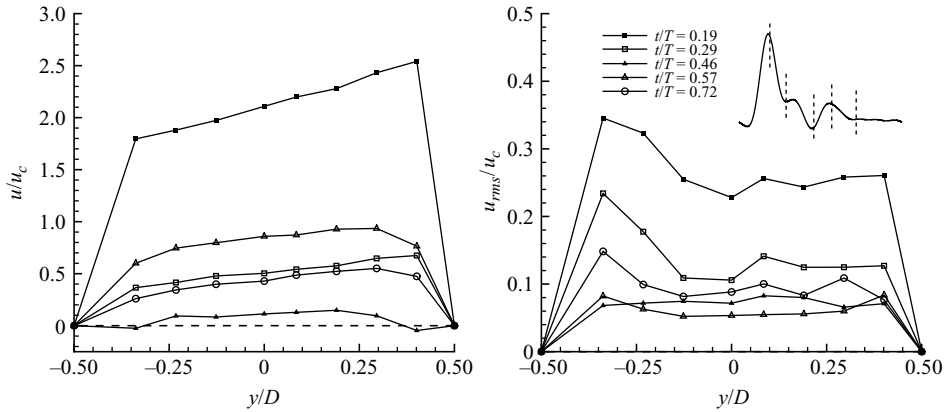


FIGURE 15. Selected mean velocity profiles  $5D$  downstream of the shear-generating insert; (a) mean velocity, (b) r.m.s. velocity fluctuation.

pulse and also that of the secondary pulse. The tertiary pulse does not decay until  $4 < x/D < 5$ , but after the tertiary pulse, the velocity drops towards the upstream value rapidly. The r.m.s. velocity magnitude for the skewed profile case is generally higher around  $x/D < 6$  as a result of the jet breakdown in this region. The peak r.m.s. velocity for the primary pulse jet occurs between  $2D$  and  $3D$ . The peak r.m.s. velocity for the tertiary pulse is centred around  $4D$ , as opposed to  $6D$  in the baseline case. In the baseline case, the r.m.s. velocity at  $x/D = 2$  is observed to be relatively small. In the skewed inlet profile case, however, the r.m.s. velocity is relatively high at this location, particularly during the primary pulse. This is the result of the earlier jet breakdown in the perturbed case.

The centreline velocity time-traces are directly compared with the baseline case in figure 17. At  $x = 2D$ , the centreline velocity profiles are similar in shape, but those for the skewed case are of lower magnitude. This may result from a slight asymmetry in the velocity profile caused by the skewed inlet. However, the skewing of the velocity profile in the near-stenosis region is small, suggesting that the discrepancy may be due to the earlier jet breakdown observed for this case. The peak velocity magnitude for the two cases are slightly shifted in figure 17 at  $2D$ , as well. This magnitude continues to drop in the range  $3 \leq x/D \leq 4$ . A spike, similar to that in the baseline case is evident at  $t/T \sim 0.15$  for the primary pulse and at  $t/T \sim 0.60$  for the tertiary pulse. The spike is most obvious at  $x/D = 5$  and  $6$ . By  $x = 10D$  there is little distinction between the velocity profiles for the two cases.

The propagation velocity of the primary and tertiary pulses can be obtained from the time derivative of the centreline velocity time-trace, as in the baseline case. The primary and tertiary pulses propagate approximately at  $12$  and  $7 \text{ cm s}^{-1}$ , respectively. The derivatives were noisier in the skewed inlet case, however, so these values are averages.

Figure 18 compares the IWF normalized velocity time-trace at several downstream locations ranging from  $x/D = 2$  to  $18$ . These data are the same as those presented in figure 17, but this normalization makes some of the differences between the two cases more apparent. Recall that for IWF normalization, fully developed flow that has recovered to the inlet velocity profile is characterized by a horizontal line at  $u_{CL}/u_{iwf} = 1$  for all phases. At  $2D$ , the baseline and skewed inlet cases are similar, with the skewed inlet resulting in a slightly lower velocity, as discussed above with respect to figure 17. The discrepancy is significantly larger by  $4D$ , with the best

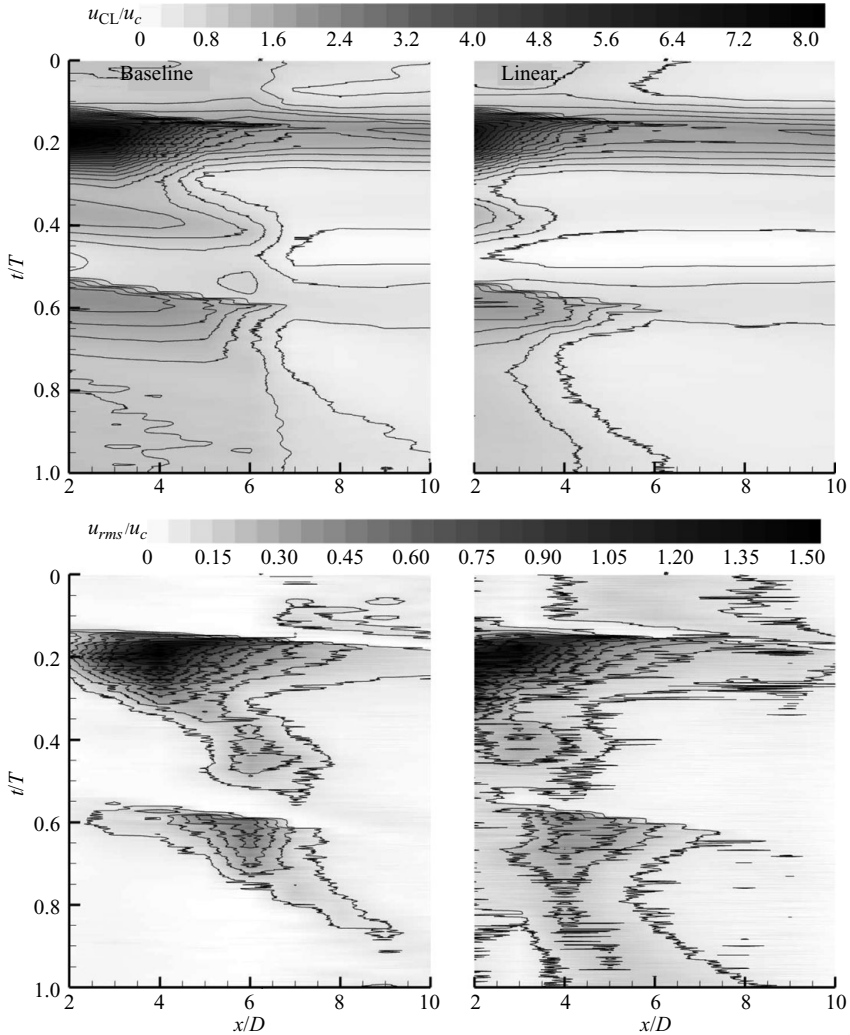


FIGURE 16. Centreline velocity contour comparison; baseline versus linear velocity profile.

agreement occurring at the primary and tertiary pulse phases. This is expected, as these are the last phases of the cycle to exhibit a strong stenotic jet. The deficit in the vicinity of  $t/T=0.45$  present in the baseline case begins to appear at  $x/D=4$  and is evident in all subsequent frames. By  $6D$ , the profile for the skewed inlet is close to  $u_{CL}/u_{iwf}=1$ , which indicates that the flow has largely relaxed to the input waveform. The stenotic jets have broken down and a spike presumably associated with the vortex ring is the only remaining artifact associated with the primary and tertiary pulses. At  $x=8D$ , the stenotic jet for the baseline case has broken down and the similarity between the two cases increases considerably. The agreement between the two time-traces continues to improve through the remainder of the test section.

Figure 19 highlights the similarities between the two cases at the downstream measurement locations ( $14D-18D$ ). The time-traces nearly coincide, including the location of ridge shown in the baseline case in figure 11. The pulse observed to propagate throughout the domain in the baseline case is also evident in the skewed

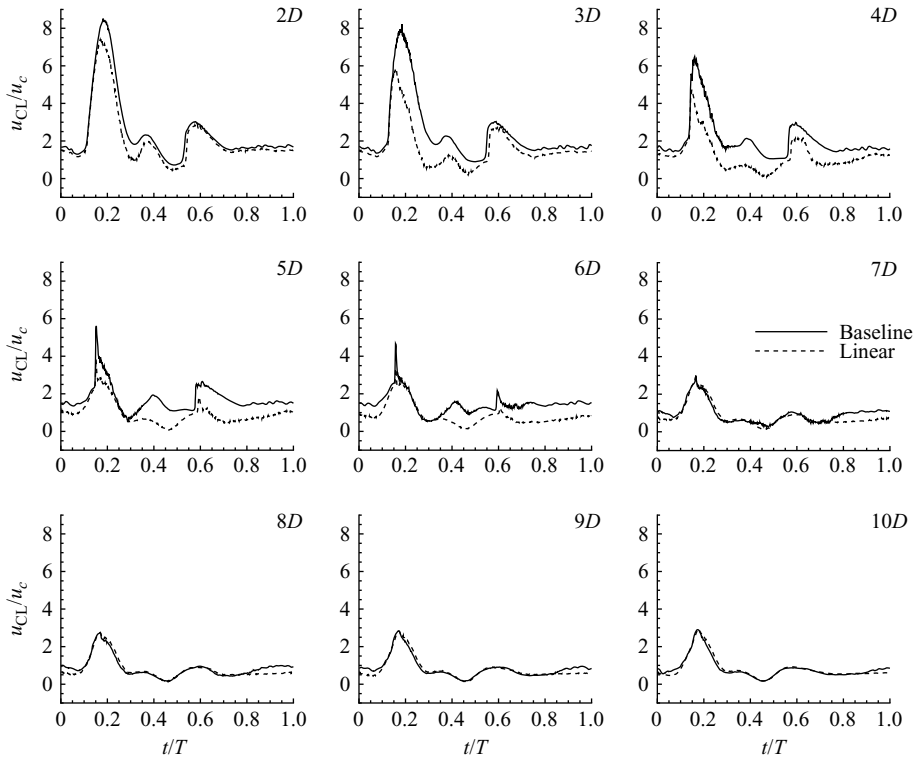


FIGURE 17. Direct comparison of centreline velocity in the skewed inlet and baseline cases.

inlet case, although it is slightly broader. Furthermore, it appears to propagate at the same rate. The difference in the peak locations is on the order of a few hundredths of a second and is thus within experimental uncertainty.

Average PIV results measured during phases corresponding to the primary pulse (figure 20) show that a vortex ring is initiated at  $t/T = 0.12$  and propagates downstream. Streamlines have been used instead of the  $Q$ -criteria for identifying the vortex ring because they better show the jet skewing. Even though the streamlines are not Galilean-invariant so that the vortex ring core identified in this manner does not coincide with the true core, they are still useful for illustrating jet trajectory. After the vortex ring passes, the stenotic jet trajectory tends to be offset towards the upper portion of the tube. The skewness in the velocity profile results in bending of the jet as follows: as the jet emanates from the stenosis and the streamlines start to diverge, it is subject to a radial pressure gradient arising from the streamline curvature. The strength of the pressure gradient is a function of the radius of curvature and the local fluid velocity squared,  $V^2/R$ . As the velocity profile is non-uniform, the resulting radial pressure gradient is non-uniform, which results in a bias of the jet trajectory towards the higher velocity side of the profile. This is clearly observed at  $t/T = 0.15$ – $0.16$ . Once the primary pulse strength is reduced, the bias is less apparent and the flow attains a skewed profile with no discernible jet. The jet does not bend appreciably for the tertiary pulse, presumably due to the lower velocity and subsequent weaker radial pressure gradient.

The circulation of the primary vortex ring computed from the instantaneous PIV data averaged  $4.4 \text{ cm}^{-2} \text{ s}^{-1}$  in the skewed inlet case, which is close to the average

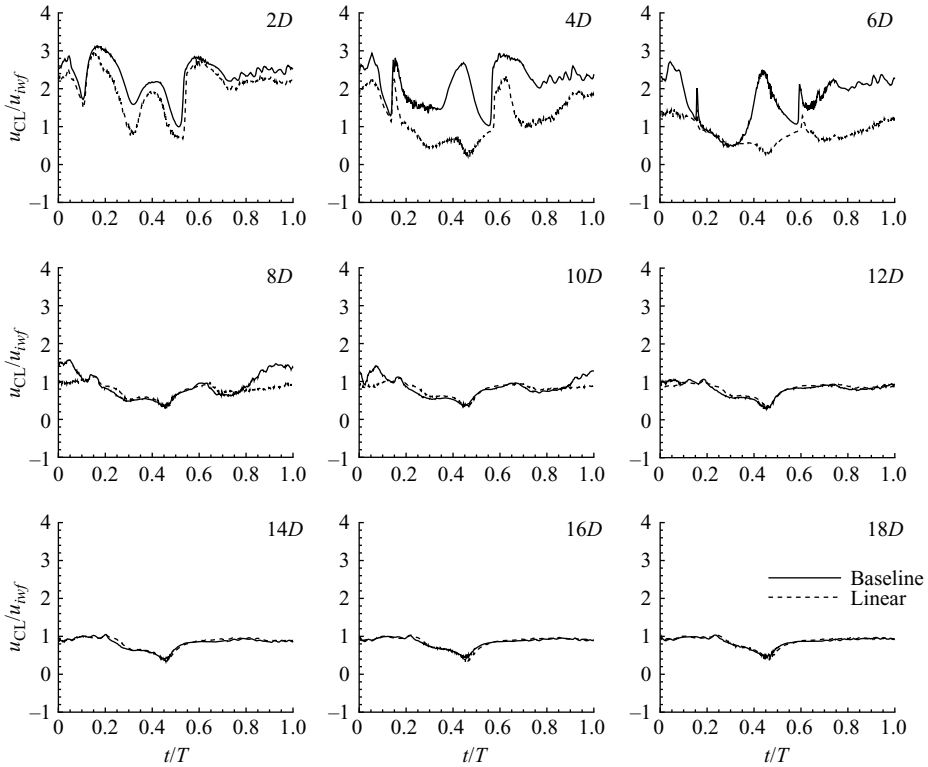


FIGURE 18. Comparison of the IWF normalized centreline velocity for the baseline and linear insert cases.

circulation of  $4.5 \text{ cm}^{-2} \text{ s}^{-1}$  in the baseline case. The tertiary vortex ring has an average circulation of  $2.5 \text{ cm}^{-2} \text{ s}^{-1}$  in the skewed inlet case, compared to  $2.8 \text{ cm}^{-2} \text{ s}^{-1}$  for the baseline case. These skewed inlet values agree with the baseline data within the uncertainty of the calculation. This suggests that skewing the inlet velocity profile does not significantly alter the vortex ring formation.

#### 4.2. $180^\circ$ bend

##### 4.2.1. Design of bend

The  $180^\circ$  bend was machined from an acrylic block at a tube radius to radius of curvature ratio  $\delta/R = 1/7$ . A schematic of the geometry is presented in figure 21. The  $1/7$  ratio was selected because of its frequent use in the existing body of literature on pulsatile flow through curved geometries. A  $180^\circ$  bend was similarly selected due to its prevalence in the literature and to ensure that both the axial and secondary flows were developed (Swanson, Stalp & Donnelly 1993). A 3 mm deep recess was machined into each end of the bend apparatus to accommodate the glass tubing, which was affixed to the bend using silicone caulk. The bend assembly was rigidly mounted to the index matching enclosure to ensure accurate positioning and stability.

The velocity profile immediately downstream of the bend (less than  $1D$ ) is presented in figure 22 for six phases (refer to figure 21 for axis orientation). The phase associated with each subplot is indicated on the waveform at the bottom of the figure. During the acceleration phase (figure 22a), the velocity profile is nearly linear over the majority of the cross-section, tapering off quickly near the walls. Just after peak flow (figure 22b),

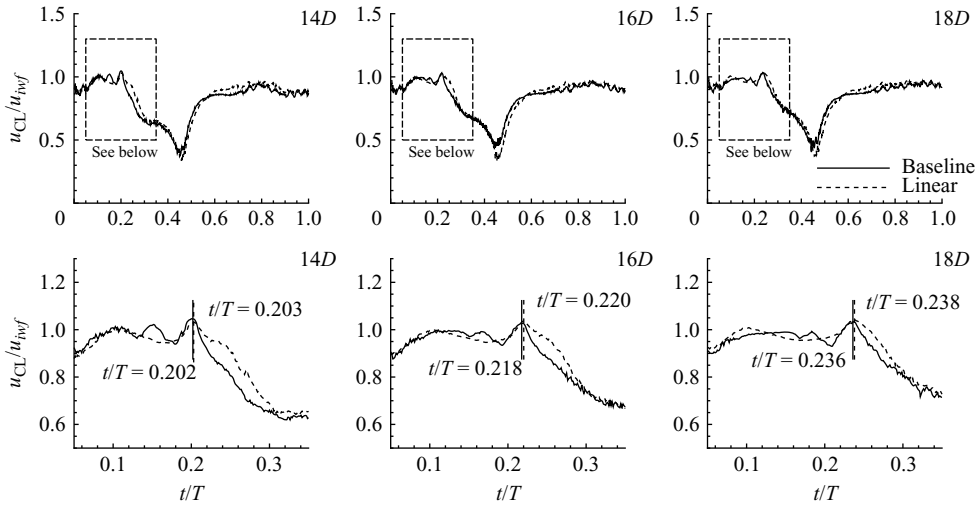


FIGURE 19. Comparison of the IWF normalized centreline velocity for the baseline and linear insert cases.

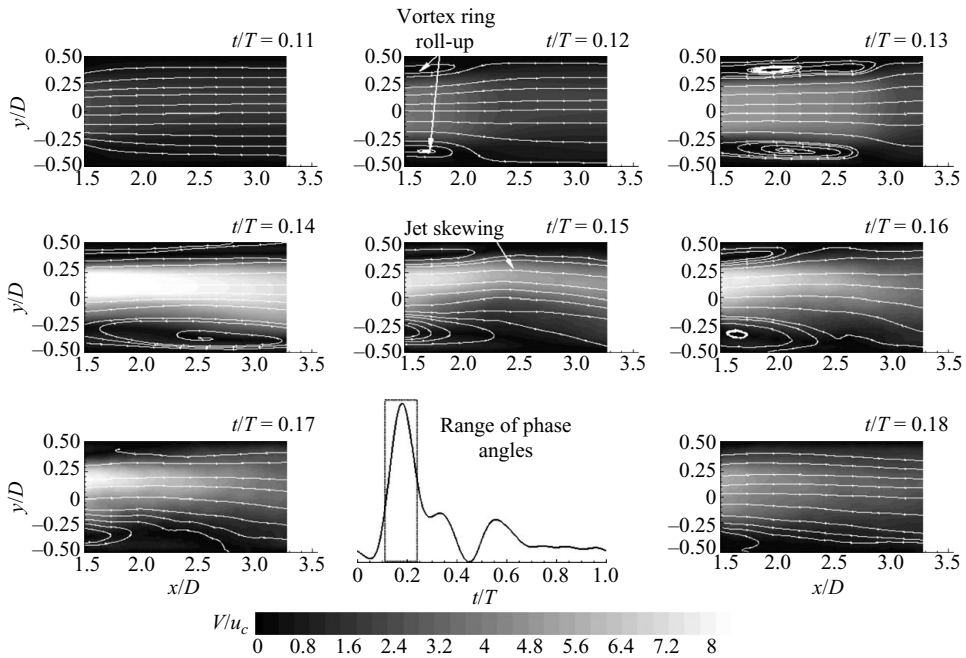


FIGURE 20. Vortex ring roll up and jet deflection of the linear insert case; mean velocity magnitude with overlaid streamlines.

the velocity near the inner radius of curvature begins to decrease resulting in a slight ‘bowl’ shape. The velocity profile retains its shape while its overall magnitude decreases during deceleration of the primary peak (figure 22c). In figure 22(c), a region of backflow is evident as the ‘bowl’ drops below zero. The ‘bowl’ shape disappears between the secondary and tertiary pulses (figure 22d), though there are still areas of reversed flow. The acceleration phase of the tertiary peak (figure 22e) results in

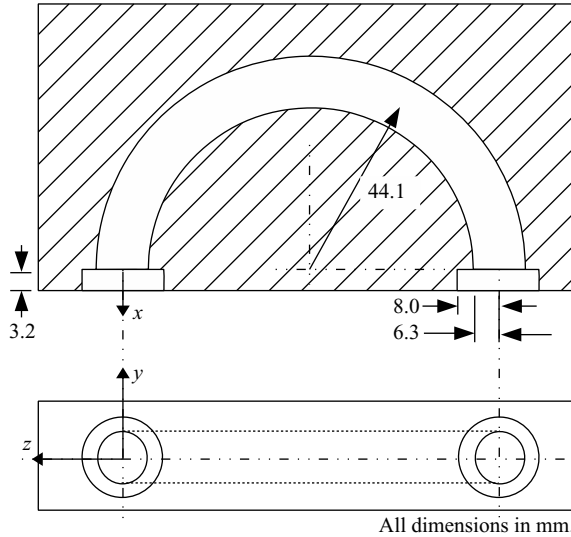


FIGURE 21. Schematic diagram of the curved test section.

a profile similar to part *a*, but with lower overall magnitude; the velocity profile is again roughly linear over the bulk of the cross-section. Figure 22(*f*) shows the velocity profile over the remainder of the cycle. It is similar to figures 22(*a*) and 22(*e*), with lower bulk velocity magnitudes. The velocity profile is more complex than that for the linear insert case during the deceleration phase. A few phases are directly compared in figure 23 to highlight the differences between the bend and linear insert cases.

The secondary flow induced by the Dean's vortices was measured along a line scan in the  $y$ -direction at  $x/D = 0.08$ . The measurement was performed off-centre because strong reflections along the centreline caused an unacceptably high signal-to-noise ratio, resulting in poor data. The results of the scan are presented in figure 24. In general, the secondary flow velocity is about an order of magnitude lower than that of the axial flow. The orientation of the Dean's vortices remains the same during the cycle, with the same sense of rotation as in steady flow. The strongest vortices occur during the primary and tertiary pulses. At other phases the secondary flow is considerably weaker. It is unknown whether multiple (Lyne-type) vortex structures arise. Given the low Womersley number, however, the unsteady inertial effects should be small and the Stokes layers should be thick. This reduces the likelihood of significant multiple vortex regimes.

#### 4.2.2. Results

The mean and r.m.s. fluctuating velocity along the tube centreline of the bend case is compared with the baseline case in figure 25. As in the skewed inlet case, the stenotic jets do not persist as far downstream in the bend case. The primary pulse velocity decays by  $x/D \sim 5$ , while the velocities at other phases decay in the  $x/D \sim 4$  region. As in the other disturbed flow case, this is a reduction relative to the baseline case of  $\sim 2D$ . The shift of the primary and tertiary pulses in the  $x/D \leq 4$  region is evident in the mean velocity (top row of plots) for the bend case. The slope appears to be similar to that of the baseline case. The r.m.s. velocities of the primary pulse in both cases are similar except that the peak location is slightly further downstream in the baseline case. The maximum r.m.s. velocity of the tertiary pulse is centred around

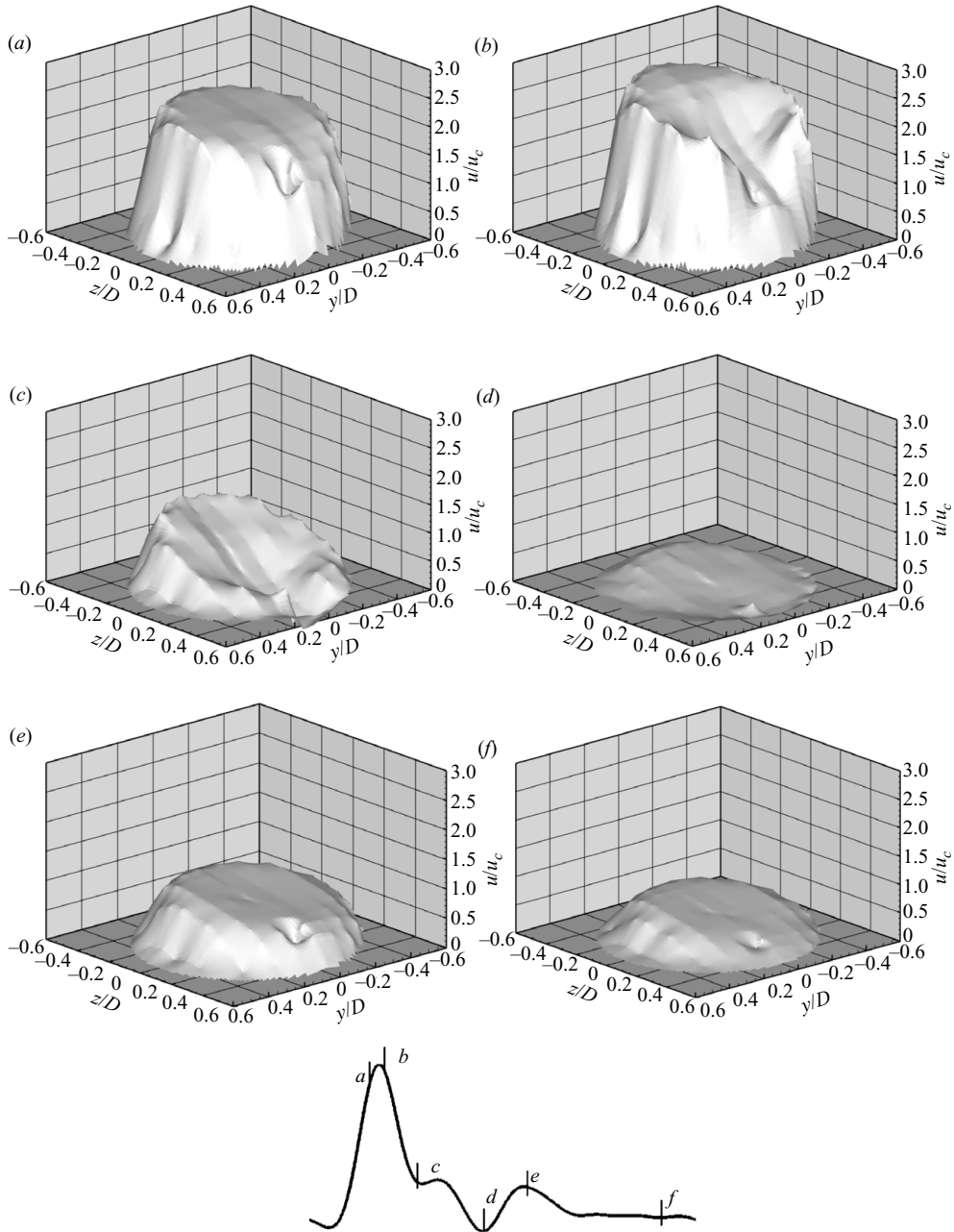


FIGURE 22. Cross-sectional velocity profiles immediately downstream of a  $180^\circ$  bend  $x/D < 1$  under physiological forcing.

$x/D=4$ , as in the linear case. This is approximately  $2D$  further upstream than the baseline case.

The time-traces of the baseline and bend cases are directly compared in figure 26. At  $2D$  the bend case velocity is slightly below that of the baseline case, although the shapes are qualitatively similar. This is similar to the skewed inlet case results, in which the centreline velocity at  $2D$  was of lower magnitude and had slightly shifted

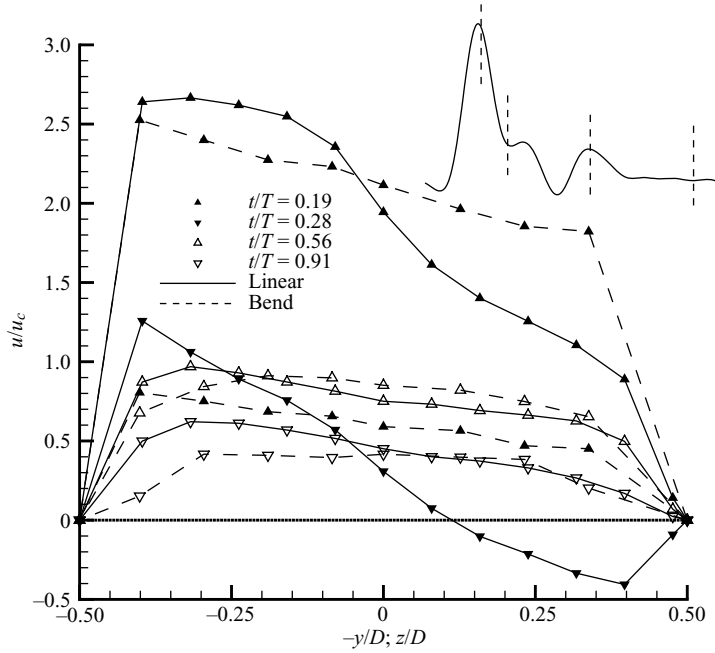


FIGURE 23. Comparison of the velocity profile produced by the linear insert and the bend at a few phases selected to highlight the differences.

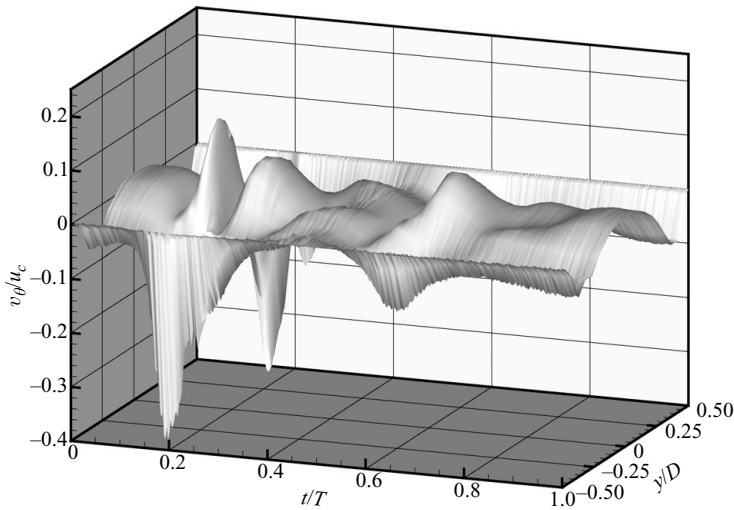


FIGURE 24. Azimuthal velocity along the line  $x/D = 0.08$ .

peaks in comparison with the baseline case. At  $3D$ , the shape of the time-trace in the two cases remains similar, but the magnitude is now considerably lower for the bend case. By  $4D$ , the bend case velocity magnitudes decrease to the order of the upstream input waveform. This is the region of high r.m.s. velocity shown in figure 25, corresponding to flow breakdown. Once the baseline flow has broken down ( $x/D \geq 7$ ), the waveforms of both cases are very similar.

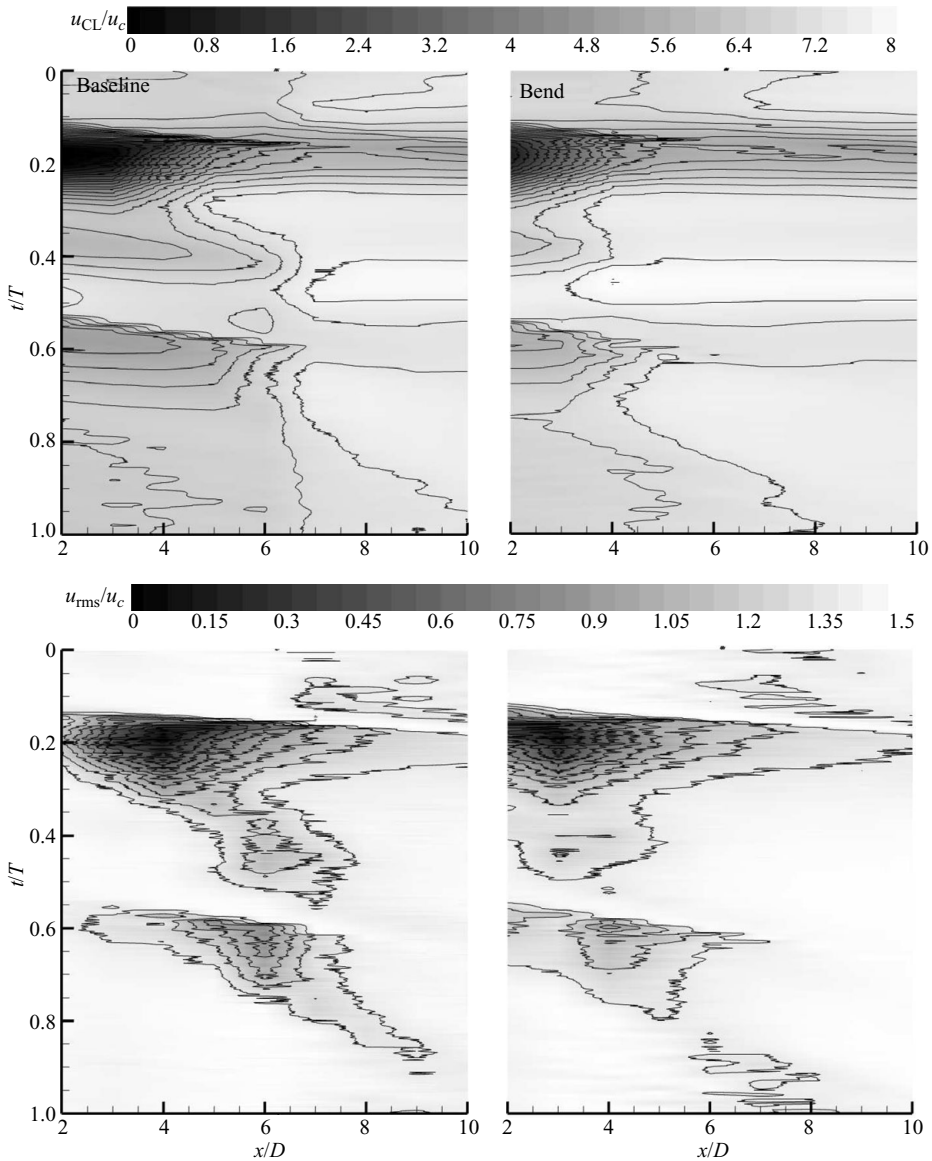


FIGURE 25. Centreline velocity contour comparison; baseline versus bend profile.

Figure 27 presents the raw centreline velocity time-traces compared to the input velocity and acceleration waveforms. The time-traces at  $2D$  and  $3D$  show that oscillations follow the primary and tertiary pulses for a significant amount of time and are very predictable. The oscillations become more erratic at  $4D$  and  $5D$  before disappearing completely further downstream. Similar oscillations were observed in the baseline case, but their amplitudes were not nearly as large. As observed in the baseline case, the oscillations begin at the peak of the acceleration waveform and grow in amplitude throughout the remainder of the acceleration phase and into the deceleration phase. The flow becomes highly erratic after the peak in the velocity waveform (i.e. during the deceleration portion of the cycle).

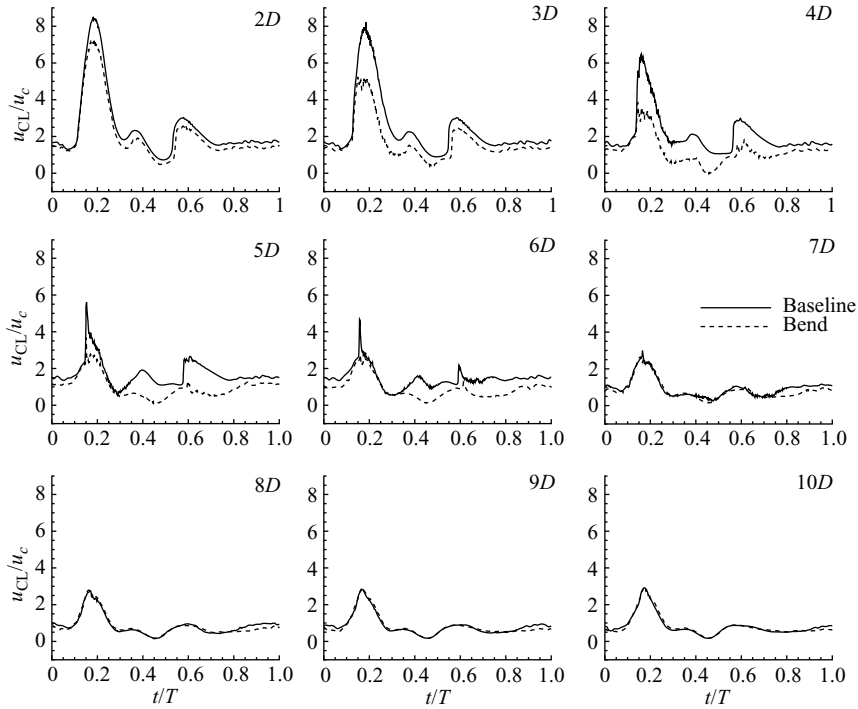


FIGURE 26. Centerline velocity comparison; baseline versus bend profile.

The pulse propagation velocity ('peak shift') was  $10.4$  and  $6.3 \text{ cm s}^{-1}$  for the primary and tertiary pulse, respectively. This is of the same order as the velocities computed in the baseline and skewed inlet profile cases, within experimental uncertainty. As in the skewed inlet case, the peaks are not evenly spaced, so the values presented are averages. The good agreement between these values and those of the skewed inlet and baseline cases suggests that the vortex ring formation is unaffected, despite the perturbations imposed by the skewed velocity profile and the secondary flow. The strong agreement between the convection velocities of these coherent structures in the three cases suggests that the radius and circulation of the vortex rings are essentially equal, which has been corroborated with PIV data.

The IWF normalized centreline velocity time-traces for the baseline and bend cases are compared at three downstream locations ( $16 \leq x/D \leq 20$ ) in figure 28. The centreline velocity in the bend case, as in the other perturbed case, has a persistent deficit near  $t/T = 0.45$ . Additionally, the propagating ridge observed in the baseline case exists in the bend case and occurs at approximately the same phase angle. Thus it propagates at the same velocity. The bend case has a velocity magnitude nearer  $u_{CL}/u_{iwf} = 1$  at all phases, meaning that it has relaxed to a fully developed velocity profile.

#### 4.3. Comparison of the skewed inlet and the skewed inlet with swirl (bend)

Insight into the effect of swirl on stenotic flow development can be obtained via direct comparison of the skewed inlet case and the flow downstream of the bend because the effects of skewing and secondary flow have been isolated by these two experiments. Figure 29 compares the IWF normalized centreline velocity time-traces

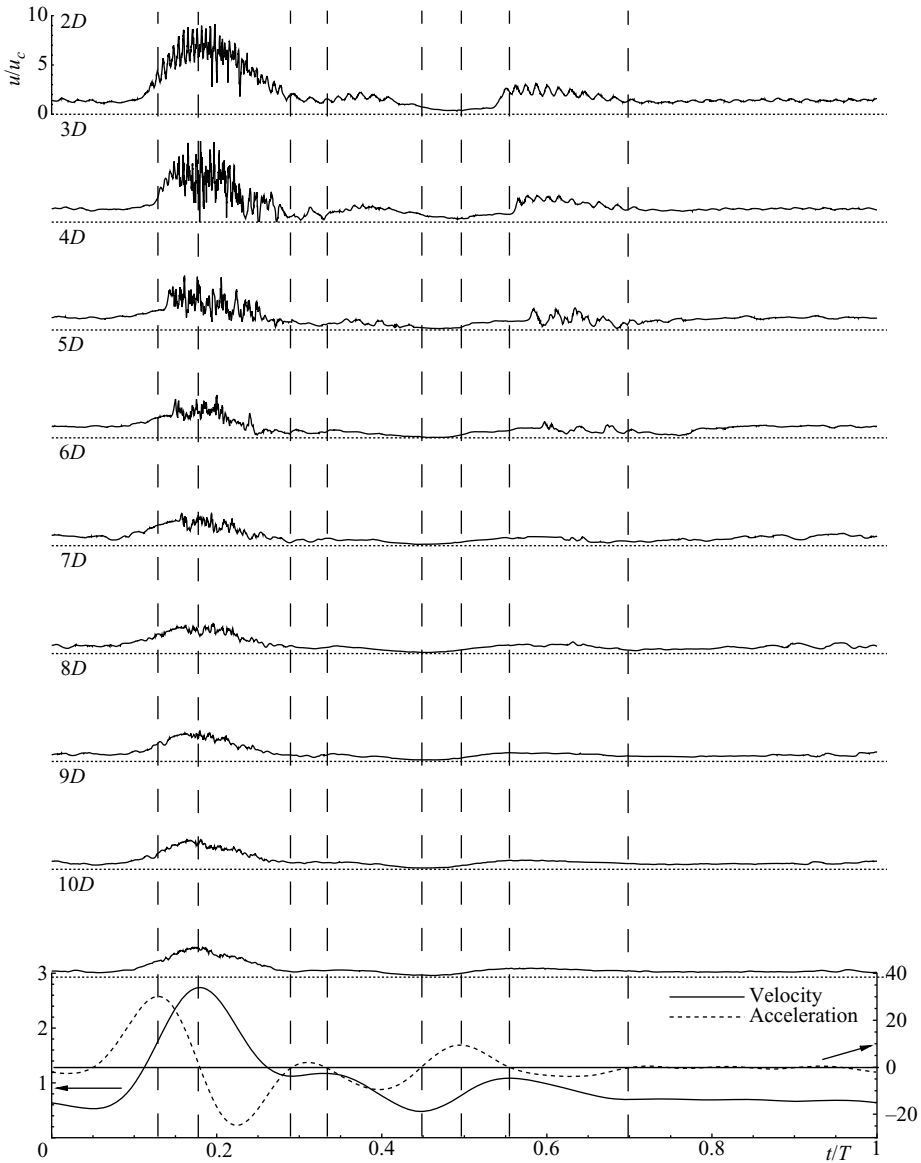


FIGURE 27. Centerline velocity time-trace comparison; bend.

for these cases. The mean velocity time traces are remarkably similar, showing only slight variation over the streamwise distance of 16 diameters. It was expected that sufficiently far downstream, all cases would relax to approximately the same centreline velocity, but even in close to the stenosis and the velocities associated with the skewed inlet and bend cases are in considerable agreement. This implies that the effect of swirl is minor compared to that of the mean velocity profile. Far downstream, presented in figure 30, the bend case velocities are slightly nearer to the upstream waveform values ( $u_{CL}/u_{iwf} = 1$ ), suggesting that over time the action of the secondary flow aids in redevelopment by enhancing momentum redistribution. Table 4 lists the average deviation of the velocity in each case from the upstream input velocity waveform at

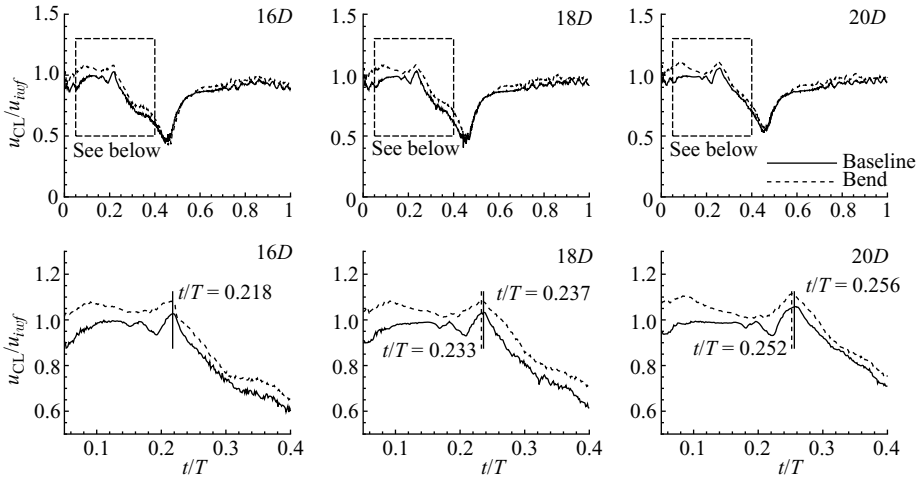


FIGURE 28. Comparison of the IWF normalized centreline velocity for the baseline and bend cases.

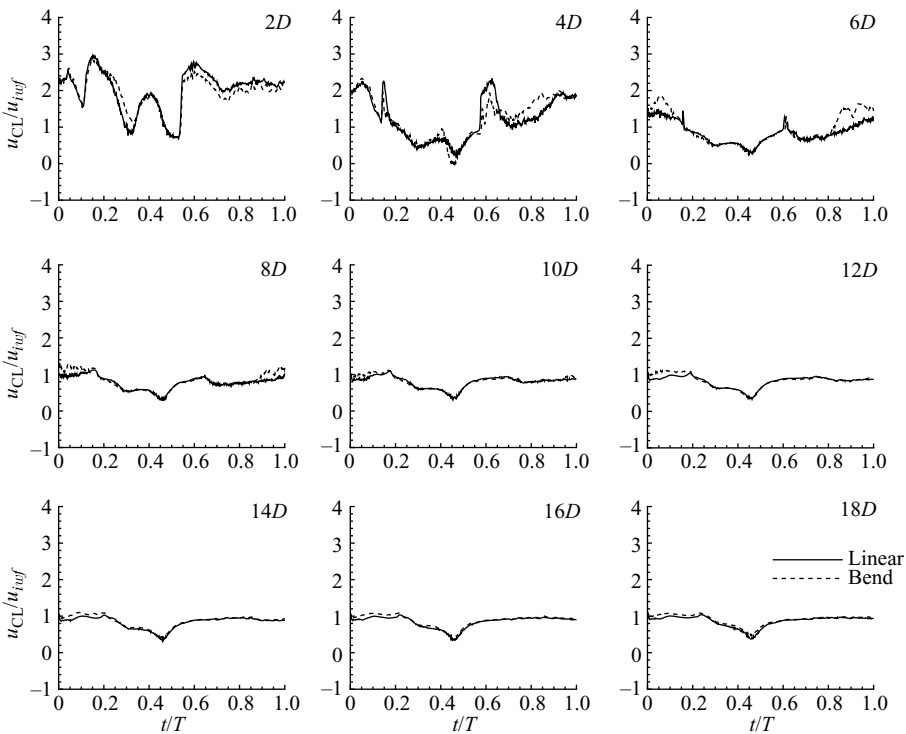


FIGURE 29. Comparison of the IWF normalized velocity time-traces of the linear insert and bend cases to highlight the effect of secondary flow.

the three locations presented in figure 30. It can be concluded from this table that far downstream, the baseline case deviates most from the fully developed profile, followed by the skewed inlet case, and the bend case. The jet breakdown in the baseline case occurs furthest downstream, so it is reasonable that the velocity field requires longer

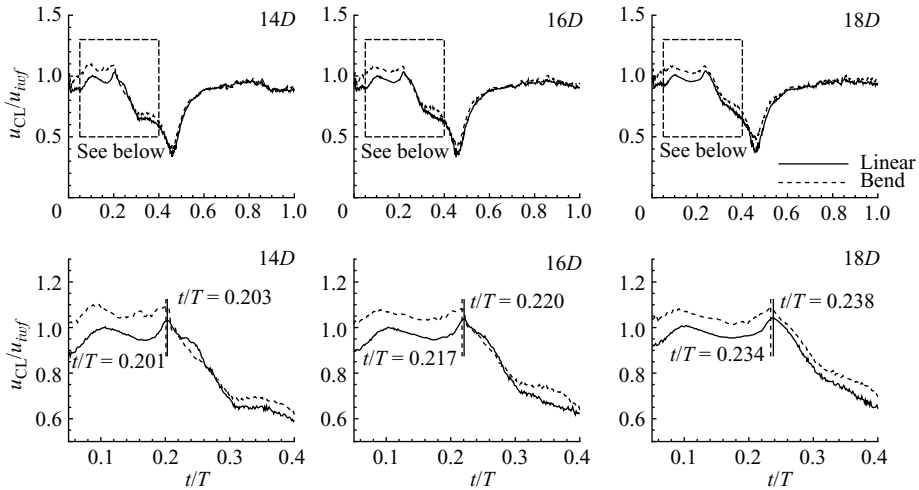


FIGURE 30. Comparison of the IWF normalized velocity time-traces of the linear insert and bend cases to highlight the effect of secondary flow; downstream.

	14D (%)	16D (%)	18D (%)
Baseline case	18.2	15.7	14.4
Skewed inlet case	16.7	15.3	13.6
Bend case	13.8	11.7	9.4

TABLE 4. Average deviation of the centreline velocity time-trace of each case from the fully developed upstream velocity time-trace far downstream.

to redevelop. The two disturbed cases break down in approximately the same region ( $\sim 2D$  upstream of breakdown in the baseline case). Although the near-field flow of the bend and skewed inlet profile cases are similar, the bend case redevelops the quickest. This is hypothesized to be a result of the mixing action of the secondary flow.

## 5. Summary and conclusions

Experimental measurements concerning the sensitivity of stenotic flows to the inlet velocity profile and secondary flows were presented. The skewed inlet velocity profile produced using the porous insert generated axial flow qualitatively similar to the flow produced via the centripetal action of the flow around the bend, in absence of secondary flow. The experiments utilized both LDV and PIV measurements to ascertain the temporal and spatial characteristics of the dominant flow features. The uncertainties in the mean velocity statistics were  $\pm 1\%$  for LDV and less than  $\pm 3\%$  for PIV data away from the walls. Uncertainties increased near the wall for both measurement techniques.

The baseline case consisted of a 75% (by area) stenosis with imposed physiological forcing (Holdsworth *et al.* 1999). Each pulse in the imposed waveform produced a stenotic jet and corresponding vortex ring that propagated downstream. The jet broke

down between 6 and 8 diameters downstream of the stenosis. The flow continued to redevelop for the remainder of the measurement region, never re-establishing the upstream profile. Vortex rings produced via the Kelvin–Helmholtz instability began shedding at the phase of the pulsatile cycle where the rate of acceleration was low. This triggered instabilities further downstream and resulted in the breakdown of the flow. The frequency at which the vortex rings peeled off was a function of the Reynolds number at that particular phase, with a higher Reynolds number corresponding to a higher frequency. Additionally, the frequency was dependent on the disturbance type.

The vortex ring produced by the primary pulse had a ring Reynolds number of approximately 450. The location of the vortex ring and its angle with respect to the tube cross-sectional plane varied slightly from cycle to cycle. A pulse appears to persist throughout the entire measurement domain and propagate downstream with a velocity close to that of the primary vortex ring. It appears to originate in a small time after the primary vortex ring. It is most assuredly not a coherent ring, as any ring structure would have long since broken down. However, it is apparent in all three cases. The vortex ring produced by the diastolic pulse has a ring Reynolds number of 280 and a consequent lower velocity. The diastolic peak did not produce a long-lived pulse.

The two perturbed inlet cases were found to reduce the extent of the coherent stenotic jet by  $\sim 2D$  ( $\sim 30\%$ ). The skewed inlet profile resulted in an asymmetric radial pressure gradient that forced the jet towards the wall. Comparison of the skewed inlet case with the flow downstream of the bend showed very little difference, implying that in the near field, the secondary flow introduced by the bend plays a lesser role than does the skewed velocity profile. It is the action of the mean flow that disrupts the stenotic jet and forces premature breakdown.

The vortex rings produced in the perturbed cases by the primary and tertiary pulses were nearly identical in strength to that produced in the baseline case. It is likely that a much stronger mean velocity gradient than the peak gradient of  $\sim 4.75 \text{ s}^{-1}$  used in this study would disrupt the vortex ring formation. The vortex ring formed and propagated downstream with little spatial bias with respect to the centreline (on average). After the vortex ring passed, the stenotic jet trajectory was skewed due to the non-uniform radial pressure gradient, as previously discussed. The symmetry of the stenosis (and mostly likely the stenosis degree) appears to be the key prerequisite for coherent vortex ring formation. The vortex ring formed by a symmetric stenosis is not very sensitive to the velocity profile and swirl upstream of the constriction.

This study demonstrated that the gross flow features of a stenotic flow, such as the extent of the downstream recirculation region and transition location, are sensitive to the upstream velocity profile. Previous work has demonstrated that these flows are also sensitive to geometric perturbations (Varghese *et al.* 2007*a,b*). Interestingly, secondary flow was found to have a minor effect on the gross flow features, suggesting that numerical models concerned with these macroscopic features need be concerned primarily with accurate inlet velocity profiles. The impact of the secondary flow may be within the noise level of the current experiments, though the secondary flow was relatively strong.

At present, cellular studies conducted in realistic geometries of stenotic vessels are in their infancy. To the authors' knowledge, only one study has attempted to characterize gene expression in a stenotic flow (McCann 2005). Her study was conducted in steady flow and the spatial resolution was very coarse because of the

large number of samples (cells) required for a reliable signal. The cellular response to the stenotic flow was investigated in two regions, one containing the recirculation region, the reattachment zone, and a portion of the relaminarization region and the other containing solely the far downstream relaminarization region. In this regard, the complexity of the current study precludes the results from direct utilization by the cellular mechanics community. As the spatial resolution of the cell studies in realistic geometries improves, however, the impact of upstream flow conditioning may be of concern to biological researchers.

## REFERENCES

- ADRIAN, R. J. 1996 Laser velocimetry. In *Fluid Mechanics Measurements*, 2nd edn. (ed. R. J. Goldstein), pp. 175–299. Washington, DC: Taylor & Francis.
- AHMED, S. A. & GIDDENS, D. P. 1983 Velocity measurements in steady flow through axisymmetric stenoses at moderate Reynolds numbers. *J. Biomech.* **16**, 505–516.
- AHMED, S. A. & GIDDENS, D. P. 1984 Pulsatile poststenotic flow studies with laser doppler velocimetry. *J. Biomech.* **17** (9), 695–705.
- BERATLIS, N., BALARAS, E., PARVINIAN, B. & KIGER, K. 2005 A numerical and experimental investigation of transitional pulsatile flow in a stenosed channel. *J. Biomech. Engng* **127**, 1147–1157.
- BERGER, S. A. & JOU, L.-D. 2000 Flows in stenotic vessels. *Annu. Rev. Fluid Mech.* **32**, 347–382.
- BERGER, S. A., TALBOT, L. & YAO, L.-S. 1983 Flow in curved pipes. *Annu. Rev. Fluid Mech.* **15**, 461–512.
- BHARADVAJ, B. K., MABON, R. F. & GIDDENS, D. P. 1982 Steady flow in a model of the human carotid bifurcation. Part I – flow visualization. *J. Biomech.* **15** (5), 349–362.
- BLACKBURN, H. M. & SHERWIN, S. J. 2007 Instability modes and transition of pulsatile stenotic flow: pulse-period dependence. *J. Fluid Mech.* **573**, 57–88.
- BORTOLOTTI, L. A., HANON, O., FRANCONI, G., BOUTOUYRIE, P., LEGRAIN, S. & GIRERD, X. 1999 The aging process modifies the distensibility of elastic but not muscular arteries. *Hypertension* **34**, 889–892.
- BRASSEUR, J. G. 1979 Kinematics and dynamics of vortex rings in a tube. PhD dissertation, Department of Aeronautics and Astronautics, Stanford University, Stanford, CA.
- CAO, J. & RITTGERS, S. E. 1998 Particle motion within *in Vitro* models of stenosed internal carotid and left anterior descending coronary arteries. *Ann. Biomed. Engng* **26**, 190–199.
- CHANDRAN, K. B. 1993 Flow dynamics in the human aorta. *J. Biomech. Engng* **115**, 611–616.
- CHANDRAN, K. B., SWANSON, W. M., GHISTA, D. N. & VAYO, H. W. 1974 Oscillatory flow in thin-walled curved elastic tubes. *Ann. Biomed. Engng* **2**, 392–412.
- DEAN, W. R. 1928 Fluid motion in a curved channel. *Proc. R. Soc. Lond. A* **121**, 402–420.
- DEPLANO, V. & SIOUFFI, M. 1999 Experimental and numerical study of pulsatile flows through stenosis: Wall shear stress analysis. *J. Biomech.* **32**, 1081–1090.
- DEWEY, C. F., BUSSOLARI, S. R., GIMBRONE, M. A. & DAVIES, P. F. 1981 The dynamic response of vascular endothelial cells to fluid shear stress. *J. Biomech. Engng* **103**, 177–181.
- DWYER, H. A., CHEER, A. Y., RUTAGANIRA, T. & SHACHERAGHI, N. 2001 Calculation of unsteady flows in curved pipes. *J. Fluid Engng* **123**, 869–877.
- ELAD, D. & EINAV, S. 2003 Physical and flow properties of blood. In *Standard Handbook of Biomedical Engineering and Design* (ed. M. Kutz), pp. 3.1–3.25. New York, NY: McGraw-Hill.
- FRANGOS, J. A., MCINTIRE, L. V. & ESKIN, S. G. 1988 Shear stress induced stimulation of mammalian cell metabolism. *Biotechnol. Bioengng* **32**, 1053–1060.
- HOLDSWORTH, D. W., NORLEY, C. J. D., FRAYNE, R., STEINMAN, A. & RUTT, B. K. 1999 Characterization of common carotid artery blood-flow waveforms in normal human subjects. *Physiol. Meas.* **20**, 219–240.
- HSIAI, T. K., CHO, S. K., HONDA, H. M., HAMA, S., NAVAB, M., DEMER, L. L. & HO, C.-M. 2002 Endothelial cell dynamics under pulsating flows: significance of high versus low shear stress slew rates. *Ann. Biomed. Engng* **30** (5), 646–656.

- HSIAI, T. K., CHO, S. K., WONG, P. K., ING, M., SALAZAR, A., SEVANI, A., NAVAB, M., DEMER, L. L. & HO, C-M. 2003 Monocyte recruitment to endothelial cells in response to oscillatory shear stress. *FASEB J.* **17**, 1648–1657.
- HYUN, S., KLEINSTREUER, C. & ARCHIE, J. P. JR. 2000 Hemodynamics analysis of arterial expansions with implications to thrombosis and restenosis. *Med. Engng Phys.* **22**, 13–27.
- KAMM, R. D. 2002 Cellular fluid mechanics. *Annu. Rev. Fluid Mech.* **34**, 211–232.
- KHALIFA, A. M. A. & GIDDENS, D. P. 1981 Characterization and evolution of poststenotic flow disturbances. *J. Biomech.* **14**, 279–296.
- KOMAI, Y. & TANISHITA, K. 1997 Fully developed intermittent flow in a curved tube. *J. Fluid Mech.* **347**, 263–287.
- KONNO, T., SATOH, Y. & TANISHITA, K. 1999 Model experiment on physiologically intermittent flow in an aortic arch. *JSME Intl J.* **42** (3), 648–655.
- KU, D. N. 1997 Blood flow in arteries. *Annu. Rev. Fluid Mech.* **29**, 399–434.
- LIN, J. Y. & TARBELL, J. M. 1980 An experimental and numerical study of periodic flow in a curved tube. *J. Fluid Mech.* **100**, 623–638.
- LONG, Q., XU, X. Y., RAMNARINE, K. V. & HOSKINS, P. 2001 Numerical investigation of physiologically realistic pulsatile flow through arterial stenosis. *J. Biomech.* **34**, 1229–1242.
- LYNE, W. H. 1970 Unsteady viscous flow in a curved pipe. *J. Fluid Mech.* **45**, 13–31.
- MCCANN, J. A., PETERSON, S. D., PLESNIAK, M. W., WEBSTER, T. J. & HABERSTROH, K. M. 2005 Non-uniform flow behavior in a parallel plate flow chamber alters endothelial cell responses. *Ann. Biomed. Engng* **33** (3), 328–336.
- MCCANN, J. M. 2005 An investigation of vascular cell responses to physiologically relevant mechanical and biochemical stimuli. Ph.D. dissertation, Department of Biomedical Engineering, Purdue University, West Lafayette, IN.
- MITTAL, R., SIMMONS, S. P. & NAJJAR, F. 2003 Numerical study of pulsatile flow in a constricted channel. *J. Fluid Mech.* **485**, 337–378.
- MITTAL, R., SIMMONS, S. P. & UDAYKUMAR, H. S. 2001 Application of large-eddy simulation to the study of pulsatile flow in a modeled arterial stenosis. *J. Biomech. Engng* **123**, 325–332.
- NARUSE, T. & TANISHITA, K. 1996 Large curvature effect on pulsatile entrance flow in a curved tube: Model experiment stimulating blood flow in an aortic arch. *J. Biomech. Engng* **118**, 180–186.
- NEREM, R. M. 1992 Vascular fluid mechanics, the arterial wall, and atherosclerosis. *J. Biomech. Engng* **114**, 274–282.
- NEREM, R. M., LEVESQUE, M. J. & CORNHILL, J. F. 1981 Vascular endothelial morphology as an indicator of blood flow. *J. Biomech. Engng* **103**, 172–176.
- OJHA, M., COBBOLD, R. S. C., JOHNSTON, K. W. & HUMMEL, R. L. 1989 Pulsatile flow through constricted tubes: An experimental investigation using photochromic tracer methods. *J. Fluid Mech.* **203**, 173–197.
- PETERSON, S. D. & PLESNIAK, M. W. 2003 Turbulent characteristics in a stenosed arterial model with relevance to atherosclerosis. In *Proc. Turbulence and Shear Flow Phenomena Meeting*. Sendai, Japan.
- RAFFEL, M., WILLERT, C. & KOMPENHANS, J. 1998 *Particle Image Velocimetry*. Berlin: Springer.
- SHERWIN, S. J. & BLACKBURN, H. M. 2005 Three-dimensional instabilities of steady and pulsatile axisymmetric stenotic flows. *J. Fluid Mech.* **533**, 297–327.
- SIOUFFI, M., DEPLANO, V. & PELISSIER, R. 1998 Experimental analysis of unsteady flows through a stenosis. *J. Biomech.* **31**, 11–19.
- SNYDER, B., HAMMERSLEY, J. R. & OLSON, D. E. 1985 The axial skew of flow in curved pipes. *J. Fluid Mech.* **161**, 281–294.
- STROUD, J. S., BERGER, S. A. & SALONER, D. 2000 Influence of stenosis morphology on flow through severely stenotic vessels: implications for plaque rupture. *J. Biomech.* **33**, 443–455.
- STROUD, J. S., BERGER, S. A. & SALONER, D. 2002 Numerical analysis of flow through a severely stenotic carotid artery bifurcation. *J. Biomech. Engng* **124**, 9–20.
- SWANSON, C. J., STALP, S. R. & DONNELLY, R. 1993 Experimental investigation of periodic flow in curved pipes. *J. Fluid Mech.* **256**, 69–83.
- TALBOT, L. & GONG, K. 1983 Pulsatile entrance flow in a curved pipe. *J. Fluid Mech.* **127**, 1–25.
- TARBELL, J. M. & PHAKIS, M. Y. 2006 Mechanotransduction and the glycocalyx. *J. Intl Med.* **259**, 339–350.

- TARBELL, J. M., WEINBAUM, S. & KAMM, R. D. 2005 Cellular fluid mechanics and mechano-transduction. *Ann. Biomed. Engng* **33** (12), 1719–1723.
- THOM, T., HAASE, N., ROSAMOND, W., HOWARD, V. J. & RUMSFELD, J. 2006 Heart disease and stroke statistics: 2006 update. a report from the american heart association statistics committee and stroke statistics subcommittee. *Circulation* **113** (6), 85–151.
- TOPPER, J. N. & GIMBRONE M. A. JR. 1999 Blood flow and vascular gene expression: Fluid shear stress as a modulator of endothelial cell phenotype. *Mol. Med. Today* **5**, 40–46.
- VARGHESE, S. S. 2006 Even small geometric perturbations impact stenotic flow development. PhD dissertation, Department of Mechanical Engineering, Purdue University, West Lafayette, IN.
- VARGHESE, S. S., FRANKEL, S. H. & FISCHER, P. F. 2007a Direct numerical simulation of stenotic flows. Part 1. steady flow. *J. Fluid Mech.* **582**, 253–280.
- VARGHESE, S. S., FRANKEL, S. H. & FISCHER, P. F. 2007b Direct numerical simulation of stenotic flows. Part 2. Pulsatile flow. *J. Fluid Mech.* **582**, 281–318.
- WEISS, J. 1991 The dynamics of enstrophy transfer in two-dimensional hydrodynamics. *Physica D* **48**, 273–294.
- WHITE, F. M. 2006 *Viscous Fluid Flow*, 3rd edn. New York, NY: McGraw-Hill.
- WOMERSLEY, J. R. 1955 Method for the calculation of velocity, rate of flow and viscous drag in arteries when their pressure gradient is known. *J. Physiol.* **127**, 553–563.